

TKK Dissertations 224
Espoo 2010

STRESS RELAXATION IN SUPPORTED METALLIC NANOSTRUCTURES

Doctoral Dissertation

Jari Jalonen



Aalto University
School of Science and Technology
Faculty of Information and Natural Sciences
Department of Applied Physics

TKK Dissertations 224
Espoo 2010

STRESS RELAXATION IN SUPPORTED METALLIC NANOSTRUCTURES

Doctoral Dissertation

Jari Jalkanen

Doctoral dissertation for the degree of Doctor of Science in Technology to be presented with due permission of the Faculty of Information and Natural Sciences for public examination and debate in Auditorium H at the Aalto University School of Science and Technology (Espoo, Finland) on the 28th of May 2010 at 12 noon.

**Aalto University
School of Science and Technology
Faculty of Information and Natural Sciences
Department of Applied Physics**

**Aalto-yliopisto
Teknillinen korkeakoulu
Informaatio- ja luonnontieteiden tiedekunta
Teknillisen fysiikan laitos**

Distribution:
Aalto University
School of Science and Technology
Faculty of Information and Natural Sciences
Department of Applied Physics
P.O. Box 14100
FI - 00076 Aalto
FINLAND
URL: <http://fysiikka.tkk.fi/en/>
Tel. +358-9-47001
Fax +358-9-470 23116
E-mail: tf-kanslia@tkk.fi

© 2010 Jari Jalakanen

ISBN 978-952-60-3148-4
ISBN 978-952-60-3149-1 (PDF)
ISSN 1795-2239
ISSN 1795-4584 (PDF)
URL: <http://lib.tkk.fi/Diss/2010/isbn9789526031491/>

TKK-DISS-2759

Edita Prima Oy
Helsinki 2010

ABSTRACT OF DOCTORAL DISSERTATION		AALTO UNIVERSITY SCHOOL OF SCIENCE AND TECHNOLOGY P.O. BOX 11000, FI-00076 AALTO http://www.aalto.fi	
Author Jari Juhani Jalkanen			
Name of the dissertation Stress relaxation in supported metallic nanostructures			
Manuscript submitted 26.03.2010		Manuscript revised 05.05.2010	
Date of the defence 28.05.2010			
<input type="checkbox"/> Monograph		<input checked="" type="checkbox"/> Article dissertation (summary + original articles)	
Faculty	Faculty of Information and Natural Sciences		
Department	Department of Applied Physics		
Field of research	Theoretical and computational physics		
Opponent(s)	Professor H. Jónsson, University of Iceland		
Supervisor	Professor T. Ala-Nissilä, Aalto University		
Instructor	Professor T. Ala-Nissilä, Aalto University		
<p>Abstract</p> <p>Ultrathin clean overlayers are often under mechanical stress because the atomic structures of the substrate and the adsorbate cannot be matched without strain. If the stress energies are comparable to the interface and surface energies, the system is heteroepitaxial. The self-assembly phenomena caused by stress release mechanisms of heteroepitaxial systems have application potential in nanotechnology.</p> <p>In this thesis we study two phenomena where the overlayer adopts a certain structure to release stress. In the first phenomenon the material forms islands on the supporting surface while in the second case the overlayer stays flat but nucleates a set of defects. The computational modeling used in the studies is based on coarse-grained, atomistic methods.</p> <p>We apply a simplified, two-dimensional model on the islands. It turns out that the model can describe all the common growth modes and the most frequent island shape agrees with the literature. According to the model, the dependence of the most likely island shape on the coverage is determined by the balance between the surface and the stress energies and it does not depend significantly on the wetting films beneath the island. One can fit the model to a simple analytic formula which is capable of reproducing the numerical calculations. It can be said that the model used in this thesis is now understood fairly well. Our preliminary studies indicate that the generalization of the model for three-dimensional nanowires are in good agreement with the two-dimensional results.</p> <p>When we investigate defect generation in flat thin films, we choose to model a specific system in detail. To study copper on the close-packed palladium surface, we pick another physical model than what was used with the islands because a model which has been specifically tailored for these two materials can be compared to the experiments directly. It turned out that the overlayer forms stacking faults already in the submonolayer coverage regime. The finding is consistent with experimental data but calls for a new interpretation for the overlayer structure.</p>			
Keywords Thin films, nanotechnology, computational physics			
ISBN (printed) 978-952-60-3148-4		ISSN (printed) 1795-2239	
ISBN (pdf) 978-952-60-3149-1		ISSN (pdf) 1795-4584	
Language English		Number of pages 58 p. + app. 36 p.	
Publisher Aalto University, School of Science and Technology, Department of Applied Physics			
Print distribution Aalto University, School of Science and Technology, Department of Applied Physics			
<input checked="" type="checkbox"/> The dissertation can be read at http://lib.tkk.fi/Diss/2010/isbn9789526031491/			

VÄITÖSKIRJAN TIIVISTELMÄ		AALTO-YLIOPISTO TEKNILLINEN KORKEAKOULU PL 11000, 00076 AALTO http://www.aalto.fi	
Tekijä Jari Juhani Jalcanen			
Väitöskirjan nimi Stress relaxation in supported metallic nanostructures			
Käsikirjoituksen päivämäärä	26.03.2010	Korjatun käsikirjoituksen päivämäärä	05.05.2010
Väitöstilaisuuden ajankohta 28.05.2010			
<input type="checkbox"/> Monografia		<input checked="" type="checkbox"/> Yhdistelmäväitöskirja (yhteenveto + erillisartikkelit)	
Tiedekunta	Informaatio- ja luonnontieteiden tiedekunta		
Laitos	Teknillisen fysiikan laitos		
Tutkimusala	Teoreettinen ja laskennallinen fysiikka		
Vastaväittäjä(t)	Professori H. Jónsson, University of Iceland		
Työn valvoja	Professori T. Ala-Nissilä, Aalto-yliopisto		
Työn ohjaaja	Professori T. Ala-Nissilä, Aalto-yliopisto		
<p>Tiivistelmä</p> <p>Erittäin ohuet puhtaat pintakalvot ovat usein mekaanisen jännityksen tilassa, koska kerrosmateriaalin ja alustan atomirakenteet eivät sopisi yhteen ilman venymistä. Mikäli kyseiseen jännitykseen varastoitunut energia on verrattavissa materiaalien rajapinta- ja pintajännityksiin, sanotaan systeemin olevan heteroepitaksiaalinen. Heteroepitaksiaalisissa systeemeissä tapahtuvat jännitystä lieventävät itsejärjestäytymisilmiöt ovat mahdollisesti hyödynnettävissä nanoteknologisesti.</p> <p>Väitöskirja tarkastelee kahta ilmiötä, jossa kerrosmateriaali mekaanista jännitystä lieventääkseen omaksuu tietyn rakenteen. Ensimmäisessä ilmiössä materiaali kasaantuu pinnalle saarekkeiksi ja toisessa materiaali pysyy litteänä kerroksena mutta muodostaa joukon hilavirheitä. Tutkimuksessa käytetyt mallit ovat karkeistettuja, atomistiseen kokoluokkaan soveltuvia laskennallisia menetelmiä.</p> <p>Väitöskirjassa sovelletaan saarekkeisiin yksinkertaista, kaksiulotteista mallia. Osoittautuu, että kaikki yleisimmät kasvumuodot sisältyvät malliin ja mallin ennustama todennäköisin saarekemuoto on yhtäpitävä kirjallisuuden kanssa. Mallin antama saarekemuodon riippuvuus kerrosmateriaalin määrästä tukee käsitystä, jonka mukaan todennäköisimmän saarekkeen leveys ja korkeus määräytyvät pintaenergian ja rakenteellisen jännitysenergian tasapainosta eivätkä saarekkeen alla olevat alustan kattavat kerrokset merkittävästi vaikuta asiaan. Malliin voidaan sovittaa kaava, joka pystyy toistamaan laskennalliset tulokset ja voidaan todeta, että väitöskirjassa käytetty malli ymmärretään nyt varsin hyvin. Alustavat tulokset saman mallin yleistyksellä kolmiulotteisille harjanteille ovat samankaltaisia kuin kaksiulotteisten saarekkeiden vastaavat tulokset.</p> <p>Liteiden ohutkalvojen hilavirheiden muodostumista tutkittaessa tarkastelukohteeksi päätettiin valita yksittäinen erityissysteemi yksityiskohtaista mallintamista varten. Valittu kuparikerros palladiumin tiheimmällä pinnalla kuvattiin toisella fysikaalisella mallilla kuin saarekkeiden tapauksessa, koska erityisesti kyseistä systeemiä varten räätälöidyllä mallilla tulokset ovat suoraan kokeisiin verrattavissa. Tutkimuksessa osoittautui, että kerrosmateriaali muodostavaa pinoamisvirheitä jo ennenkuin materiaalin määrä riittää kattamaan alustan pinnan. Löytö on yhteensopiva kokeellisen aineiston kanssa mutta haastaa aineiston aikaisemman tulokinnan.</p>			
Asiasanat Ohutkalvot, nanoteknologia, laskennallinen fysiikka			
ISBN (painettu)	978-952-60-3148-4	ISSN (painettu)	1795-2239
ISBN (pdf)	978-952-60-3149-1	ISSN (pdf)	1795-4584
Kieli	Englanti	Sivumäärä	58s. + liit. 36 s.
Julkaisija Aalto-yliopiston teknillinen korkeakoulu, teknillisen fysiikan laitos			
Painetun väitöskirjan jakelu Aalto-yliopiston teknillinen korkeakoulu, teknillisen fysiikan laitos			
<input checked="" type="checkbox"/> Luettavissa verkossa osoitteessa http://lib.tkk.fi/Diss/2010/isbn9789526031491/			

Preface

The work reported in this thesis has been prepared in Multiscale statistical physics group, a part of the Computational Nanoscience (COMP) group, an Academy of Finland Center of Excellence, at Aalto University School of Science and Technology. I am especially grateful to Professor T. Ala-Nissilä for giving me the opportunity to pursue doctoral studies in his group, for suggesting the topic and providing me with all the necessary facilities.

I'm indebted to Professors See-Chen Ying, Enzo Granato and Oleg Trushin for many indispensable discussions, support and wise guidance during our collaboration. I would also like to express my appreciation for the warm hospitality that Professor Ying showed me during my visits to the Brown University. I also thank Prof. Ken Elder for introducing me the Phase Field Crystal model and Dr. Giulia Rossi for sharing her insights into thin film modeling.

Financial support from the Viljo, Yrjö, Kalle Väisälä Foundation, the Finnish Cultural Foundation, the Academy of Finland, the National Graduate School in Materials Physics and the National Graduate School in Nanoscience and computer resources from the Center of Scientific Computing are gratefully acknowledged. Finally, I want to thank all the former and present members of the COMP for the past years.

Espoo, April 2010,

Jari Jalkanen

Contents

Abstract	i
Tiivistelmä	iii
Preface	v
Contents	vii
List of publications	ix
Author's contribution	x
List of abbreviations	xi
1 Introduction and motivation	1
1.1 Introduction	1
1.2 Density of states in nanostructures	4
1.3 Chemical potential and crystal shapes	5
1.4 Growth modes	9
2 Theory and methods	11
2.1 Molecular dynamics	11
2.2 Lennard-Jones pair potential	14
2.3 Embedded Atom Method	16
2.4 Activation-minimization procedure	18
2.5 Repulsive Bias Potential	19
2.6 Nudged Elastic Band-method	20
2.7 Phase Field Crystal model	22

3 Results: Islands	25
3.1 Heteroepitaxial stress release and islands	25
3.2 Two-dimensional islands	27
3.3 Island shapes at low coverage	29
3.4 Island relaxation and energy	30
3.5 Global phase diagram	33
3.6 Optimal island shape and size	34
3.7 Comparison of 2D and 3D results	35
4 Results: Overlayers	39
4.1 Dislocations and the fcc(111) surface	39
4.2 Shockley partials and stacking domains	40
4.3 Pseudomorphic overlayers	43
4.4 Stacking domains and incorporation	43
4.5 Comparison to experimental findings	46
4.6 Relaxation of several overlayers	47
5 Summary and outlook	49
Appendix:	53
Chemical potential near a surface	53
Bibliography	55

List of publications

This thesis consists of an overview and the following publications:

- I. J. Jalkanen, O. Trushin, E. Granato, S.C. Ying, and T. Ala-Nissila, “*Equilibrium shape and dislocation nucleation in strained epitaxial nanoislands*”, *Physical Review B* **72**, 081403(R):1-4 (2005).
- II. J. Jalkanen, O. Trushin, K. Elder, E. Granato, S.C. Ying, and T. Ala-Nissila, “*Two approaches to dislocation nucleation in the supported heteroepitaxial equilibrium islanding phenomenon*”, *Journal of Physics: Conference Series* **100**, 072043-072046 (2008).
- III. J. Jalkanen, O. Trushin, E. Granato, S.C. Ying, and T. Ala-Nissila, “*Equilibrium shape and size of supported heteroepitaxial nanoislands*”, *European Physical Journal B* **66**, 175-183 (2008).
- IV. O. Trushin, J. Jalkanen, E. Granato, S.C. Ying, and T. Ala-Nissila, “*Atomic studies of strain relaxation in heteroepitaxial systems*”, *Journal of Physics: Condensed Matter* **21**, 084211 (2009).
- V. J. Jalkanen, G. Rossi, O. Trushin, E. Granato, T. Ala-Nissila, and S.C. Ying, “*Stress release mechanisms for Cu on Pd(111) in the submonolayer and monolayer regimes*,” *Physical Review B* **81**, 041412(R) (2010).

Author's contribution

The author has had an active role in all the phases of the research reported in this thesis. In Publication I he did all the calculations except those concerning dislocation nucleation in large islands. All the calculations and the first draft for Publication II were done by the author. In Publication III the author performed all the calculations, had an active role in planning the calculations and interpreting the results and participated extensively in the writing of the first draft. The author participated in the overlayer studies of Publication IV and is responsible for most of the island results. The author played a central role in writing of the first draft for Publication V and did all except the Basin Hopping Global Optimization calculations. In Publication V the author had the main responsibility for planning the calculations and interpreting the results.

List of abbreviations

1D	One-dimensional
2D	Two-dimensional
3D	Three-dimensional
EAM	Embedded Atom Method
fcc	Face centered cubic
FM	Frank van der Merwe
GPD	Global Phase Diagram
hcp	Hexagonal close-packing
LJ	Lennard-Jones
MD	Molecular dynamics
MDC	Molecular Dynamics Cooling
NEB	Nudged Elastic Band
PEB	Plain Elastic Band
PFC	Phase Field Crystal
RBP	Repulsive Bias Potential
RHEED	Reflection High Energy Electron Diffraction
SK	Stranski-Krastanov
VW	Volmer-Weber

Chapter 1

Introduction and motivation

1.1 Introduction

Biological organisms can harvest resources, repair damages or build and destroy structures of human size using tools which are too small to be resolved by the eye. Manufacturing small devices in the same size scale out of inorganic materials, in the same way as the common industrial and household machinery are made, seems to be extremely difficult or impossible.

This difficulty is related to the hardness of metals and semiconductors. Unlike in biological or soft matter, the interactions between atomic constituents are much larger than $k_B T$ at room temperature. The lattice formation tendency is so strong that it generally makes most designed arrangements of atoms unstable which in turn is a major obstacle for using ordinary processing techniques in nanofabrication.

At atomistic scales, the properties of known stable nano-objects are drastically different from the properties of similar macroscopic bodies. The opportunities to employ these novel properties are under intense research at the moment [1, 2, 3, 4, 5, 6, 7]. Various devices specifically relying on the nanoscale peculiarities have already been designed. In wide-spread technological use, it would be desirable if the operation of the device were robust against disturbances. Self-assembling metallic surface structures, the topic of this thesis, can be counted to be in this category.

In general, nanoclusters have a wide range of existing and potential applications. For instance aerosols in the atmospheric science [8], metallic powders used in sintering [9] or small magnetic memory elements [10, 11] can be viewed as such. In the next paragraphs a few other interesting uses will be introduced.

A hollow nanoparticle capable of acting as a drug delivery vessel would be a great tool in medical context. Often drugs consist of small molecules which have a tendency

to spread to all tissues causing adverse side effects. The idea would be to engineer the hull of the nanocontainer in such a manner that once the container finds its way to the surroundings of the target tissue, a trigger mechanism opens the hull and the medicine becomes released.

When the particles are adsorbed on a surface, they typically alter the properties of the surface completely. A special example is the lotus-leaf effect, where self-assembled mesoscopic titanium oxide particles turn the underlying surface superhydrophobic and at the same time catalyze the decomposition of hydrogen, oxygen and carbon containing compounds into water and carbon dioxide. These two effects together are the reason why titanium oxide coated surfaces are said to be self-cleaning.

Both flat overlayers and nanoparticles are generally useful in surface coatings. Typically, a flawless epitaxial film can provide a well-defined set of energy levels which may be needed for lasers or for solar panels. On the other hand, nanoparticles practically always come with a size distribution and thus they can produce for instance white light. Nowadays their size distribution can be made extremely narrow and consequently they can compete in performance with large monocrystalline films.

Metallic thin films are already in use to boost catalysis. Many of the utilizable metals are relatively expensive and the most obvious advantage of keeping overlayer thin is to lower the costs. Often high selectivity is beneficial in catalysis. However, in catalytic converters one wants to get rid of as many burning products as possible with a single stage and therefore high selectivity is not a priority in this case. A combination of two different metals usually reduces the selectivity and in this exceptional case it leads to higher purity of the end products.

The yield of a catalytic device is often improved by patterning. In a heteroepitaxial system the equilibrium lattice constants of the substrate and the overlayer differ enough to cause significant intrinsic stresses. Usually this requires a relative lattice constant difference, i.e. misfit, above 2%. If the stress is high enough, the adsorbate can create self-assembled structures to release the strain. One advantage of these structures is that they increase the reaction-capable surface area.

Self-assembled island structures of heteroepitaxial systems have attracted a lot of research interest in recent years [11, 12, 13, 14, 15, 16, 17, 18, 19, 10, 20]. Coherent surface structures would often be preferable in many applications because dislocations can introduce spurious electronic states and they can act as trapping centers for charge carriers. There are several mechanisms which can lead to coherent arrays of islands. The question whether the surface and stress energies can balance each other and lead to island arrays has been discussed extensively. In this thesis we will show that this balance can be reached even in very simple models.

The structure of the thesis is the following. In the introduction we shall briefly look at the density of states in metallic materials and look how it changes when the dimensions

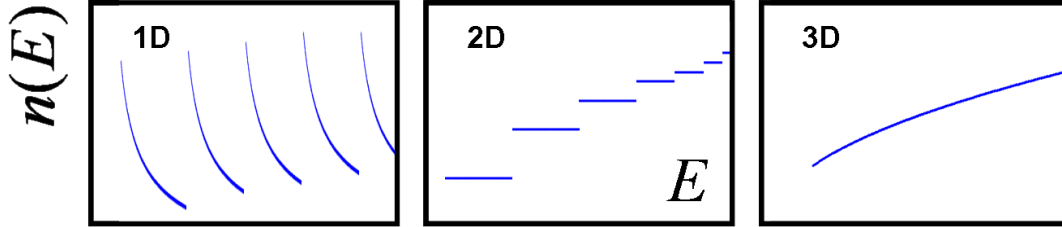


Figure 1.1: The density of states $n(E)$ depends on the dimensionality of the structure containing the particles. When the structure is so small in some dimensions that the quantum numbers in the corresponding directions do not form a proper continuum, the effective dimension of the structure can be less than 3.

of the metallic object are brought to nanoscale. We shall not investigate the electronic properties in detail. Next we introduce the chemical potential and study its relation to the crystal shapes. This section follows closely the presentation of Pimpinelli *et al.*[21]. At the end of the introduction we present a commonly used classification for growth modes of overlayers.

The methods chapter describes the computational tools used in Publications 1-5. We discuss the general idea behind the molecular dynamics method, introduce the interaction models and the specific techniques which we use to search for transition pathways and energy barriers.

Our first assortment of results deals with island formation pathway to the stress release. The island results are calculated with a very simple two-dimensional model which has only two parameters and which can be easily modified to explore the balance between stress and surface energies. It is well-known that this particular model can give only qualitative results and thus it can be considered as a minimal model for the island shapes and growth modes. At the end of the chapter we briefly look how the results would change in a three-dimensional (3D) generalization of the model. All the results except those in the 3D section are published in Publications 1-4.

In the second set of results we discuss the stress release in flat overlayers. This time we resort to a more realistic tool which is capable of reproducing many material properties correctly and which has been successful in comparisons with experiments. We do not want to consider stress relaxation by alloying and therefore we choose to model the non-mixing Cu/Pd(111) overlayer system whose applications are in catalysis. The Cu/Pd(001) is known to form islands [22] but the $\{111\}$ surface is known to stay flat [23, 24, 25]. Our calculations reveal an interesting dislocation structure in the submonolayer coverage

regime which calls for a new interpretation of the existing measurement data. These results have been published in Publication 5. In the last section we take a short look at the thicker overlayers on which we also did some generic studies in Publication 4.

1.2 Density of states in nanostructures

The metals are a large group of elements in the left-hand side of the periodic table. The alloys of these elements are also counted as metals. Quite often these metallic materials have a lattice structure, at least locally, and their properties are dominated by the nearly-free valence electrons. The nuclei and strongly bound core-electrons can be thought to form a periodic background potential, on which the electrons are spread. We explore this a little more in section 2.3. The density of states (DOS) $n(E)$ is the fraction of electrons at a certain energy E out of all electrons. The integral of DOS over all E is the total number of electrons. Instead of all the states, we can look at the DOS for the valence electrons only.

If a rectangular piece of metal has a nanoscopic diameter in x , y or z direction while the diameters in the other directions have macroscopic length L , the quantum numbers associated with the nanoscopic directions usually can not be approximated by a continuum. If there are sizable gaps between the quantum numbers of the compact directions and the geometry does not impose more topological connections between them and the other quantum numbers, the nearly-free conduction electrons can be thought to form a low-dimensional gas in the first approximation.

The semi-classical density of states (DOS) in the macroscopic dimensions d is

$$(1.1) \quad n(E) = \frac{2}{h^d N!} \int d^d V \int d^d V_p \delta(E - \frac{p^2}{2m})$$

where E is the difference of the total energy of the nearly-free particle and the energy contribution of the compact direction, the factor 2 comes from the spin-degeneracy and $d^d V$ and $d^d V_p$ are the d -dimensional volume elements in coordinate and momentum spaces. The number of particles is N and h is the Planck's constant. The Laplace transform of $n(E)$ is

$$(1.2) \quad \frac{2L^d}{h^d N!} \int d^d \mathbf{p} e^{-s \frac{p^2}{2m}} = \frac{2L^d}{h^d N!} \left(\frac{2\pi m}{s} \right)^{d/2}.$$

The DOS can be recovered from this with the help of Laplace transform tables,

$$(1.3) \quad n(E) = \frac{2 (2m\pi)^{d/2} L^d E^{d/2-1}}{h^d N! \Gamma(d/2)}.$$

Table 1.1: Single particle density of states $n(E)$ in low dimensions.

Dimension	Realization	$n(E)$
1	Nanowire	$L\sqrt{\frac{m}{E}}$
2	Quantum well	mL^2
3	Bulk	$L^3\sqrt{m^3 E}$

The general shape of the DOS in low dimensions is plotted in Fig. 1.1. In 1D and 2D cases the DOS jumps whenever there is enough energy to excite a new band from the confined direction. In a 2D quantum well the DOS has steps and in a 1D nanowire the DOS decreases with the energy. If even the last dimension of the system were shrunk to nanoscale, we would get an artificial atom where the DOS would consist of peaks, like in a real atom.

Besides the unrealistic dispersion relation, the above way of counting the states does not take into account the Pauli exclusion principle for fermions which forbids two particles to be in the same state. Thus, at best the above calculation is only a rough estimate for electrons. For phonons the expressions might be more successful. Despite these shortcomings, the general picture is in line with observations.

1.3 Chemical potential and crystal shapes

In problems involving shape or phase changes or growth, chemical potential μ is one of the most central thermodynamic quantities. In these problems the system is typically out of equilibrium and chemical potential needs to be defined locally, as a function of coordinates.

If some amount of adsorbate has been deposited on a surface in vacuum, the number of atoms N is fixed and the substrate acts as a heat bath. The natural thermodynamic potential in this case would be the Helmholtz free energy

$$(1.4) \quad F = \mu_0 N + \langle \epsilon_{\text{ad}} \rangle A,$$

where μ_0 is the constant equilibrium chemical potential and $\langle \epsilon_{\text{ad}} \rangle$ is the average surface energy for the area A .

Generally the surface free energy ϵ_{ad} is anisotropic and the average in the second term is

$$(1.5) \quad \langle \epsilon_{\text{ad}} \rangle = \frac{\int dA(\mathbf{n}) \epsilon_{\text{ad}}(\mathbf{n})}{A},$$

where the normal of the surface $z(x, y)$ over the (x, y) -plane is

$$(1.6) \quad \mathbf{n} = (n_x, n_y, n_z) = \frac{(-\partial_x z, -\partial_y z, 1)}{\sqrt{1 + (\partial_x z)^2 + (\partial_y z)^2}}.$$

Here the height function z is the difference of smallest and largest distances of points projected onto the same point in the (x, y) -plane. The projection of the surface area element on the (x, y) -plane equals $dA(\mathbf{n}) = dx dy / n_z$.

It is convenient to introduce the projected surface energy density ϕ

$$(1.7) \quad \phi = \frac{\epsilon_{\text{ad}}(\mathbf{n})}{n_z} = \epsilon_{\text{ad}}(\partial_x z, \partial_y z) \sqrt{1 + (\partial_x z)^2 + (\partial_y z)^2}.$$

We relate the system volume to the the particle number by $V = vN$, where v is an atomic volume. This can be understood for instance by introducing a reference lattice structure where almost every atom lies inside a cell of volume v . Possible deviations from this structure can be introduced as strain fields which we now neglect. In this setting $N = V/v = \int dx dy z(x, y)/v$, where the integral is assumed to be taken over the projected surface area.

Thus, the free energy has the functional form

$$(1.8) \quad F = \int dx dy \left[\frac{\mu_0}{v} z(x, y) + \phi(\mathbf{n}) \right].$$

As shown in the appendix, the chemical potential is the variational derivative of the free energy,

$$(1.9) \quad \mu = \mu_0 - v \left(\partial_x \frac{\partial \phi}{\partial(\partial_x z)} + \partial_y \frac{\partial \phi}{\partial(\partial_y z)} \right).$$

The shape of the particle stops changing when the chemical potential is a constant along the surface.

Let us denote

$$(1.10) \quad \delta\mu = \mu - \mu_0 = -v \nabla \cdot \left(\frac{\partial \phi}{\partial(\partial_x z)}, \frac{\partial \phi}{\partial(\partial_y z)} \right) \equiv -v \nabla \cdot \nabla_{\nabla} \phi.$$

Integrate both sides over the volume,

$$(1.11) \quad \int dV \delta\mu = \int dA \mathbf{n} \cdot \mathbf{r} \delta\mu = -v \int dV \nabla \cdot \nabla_{\nabla} \phi = -v \int dA \mathbf{n} \cdot \nabla_{\nabla} \phi.$$

This holds for any shape A with normal \mathbf{n} , and therefore

$$(1.12) \quad \mathbf{r} \delta\mu = -v \nabla_{\nabla} \phi.$$

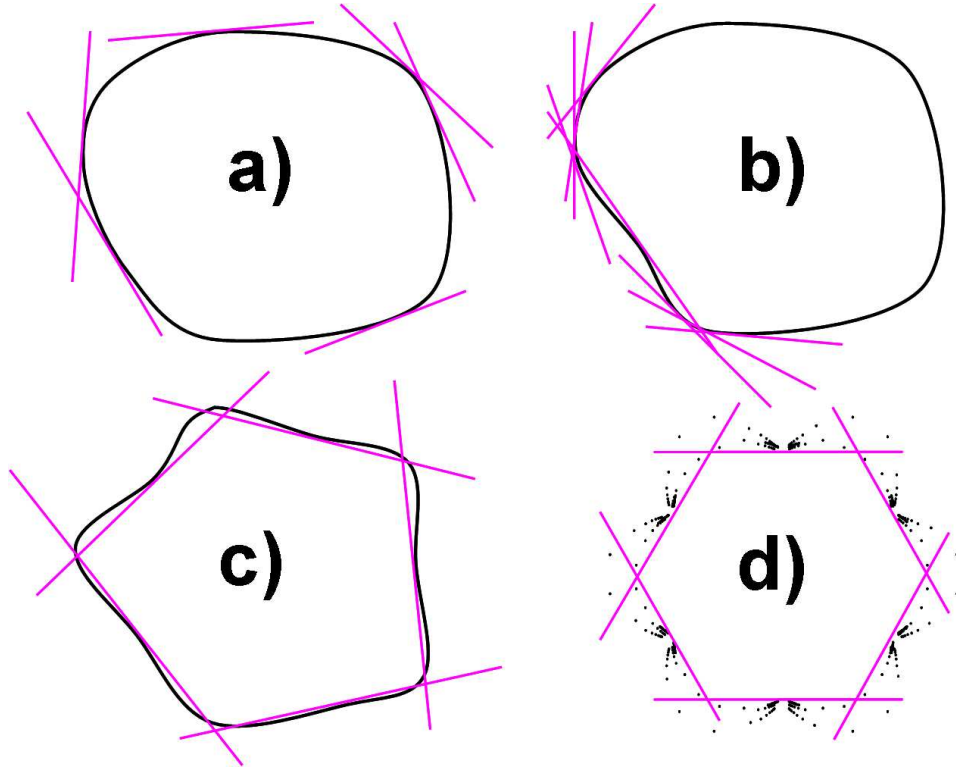


Figure 1.2: The panels a)-d) show various surface energy density ϵ_{ad} plots. The equilibrium shape is the area inside the tangent lines and ϵ_{ad} . In the first panel the shape is congruent with the ϵ_{ad} , in panel b) one low value of ϵ_{ad} causes faceting in one direction and in c) the crystal is faceted in all directions. Panel d) shows a surface energy density from a bond-counting argument and the resulting stable shape.

Multiplication of both sides with

$$(1.13) \quad \begin{pmatrix} \partial_x^2 z & \partial_{xy}^2 z \\ \partial_{xy}^2 z & \partial_y^2 z \end{pmatrix}$$

turns the left-hand side into

$$(1.14) \quad \begin{aligned} & (x\partial_x^2 z + y\partial_{xy}^2 z, y\partial_y^2 z + x\partial_{xy}^2 z) = \\ & = (\partial_x(x\partial_x z + y\partial_y z) - \partial_x z, \partial_y(y\partial_y z + x\partial_x z) - \partial_y z) \\ & = \nabla(x\partial_x z + y\partial_y z - z), \end{aligned}$$

where the parts which have only z vanish. The right-hand side becomes

$$(1.15) \quad v \frac{\partial(\partial_x z)}{\partial x} \frac{\partial \phi}{\partial(\partial_x z)} + \frac{\partial(\partial_y z)}{\partial y} \frac{\partial \phi}{\partial(\partial_y z)} = v \nabla \phi.$$

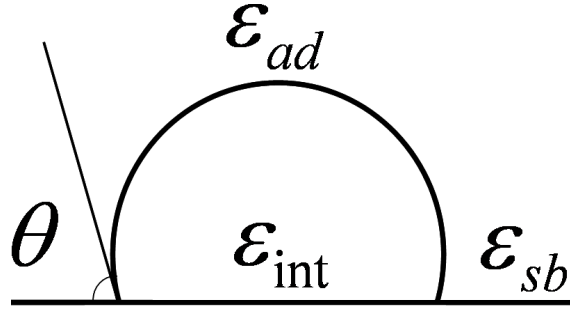


Figure 1.3: The contact angle between a liquid droplet and a supporting surface is known as Young's angle. It depends on the surface tensions between the liquid and vacuum ϵ_{ad} , liquid and the surface ϵ_{int} and the surface and the vacuum ϵ_{sb} .

Again, integrating both sides over the volume and using the Stokes theorem gives a surface integral which has to be valid for any A and the associated \mathbf{n} . Thus,

$$(1.16) \quad v\phi = \delta\mu(z - x\partial_x z - y\partial_y z),$$

where \mathbf{r} is a point on the surface. This can be written simply as $v\epsilon_{ad}(\mathbf{n}) = \delta\mu(\mathbf{r} \cdot \mathbf{n})$.

According to Eq. 1.16, if a tangent plane is drawn at a point on the crystal surface and a line parallel to the normal at the point is drawn from the chosen origin, the distance between the origin and the crossing point of the line and the plane equals $\epsilon_{ad}v/\delta\mu$. If we are given a surface energy function ϵ_{ad} , we can plot it in spherical coordinates for all \mathbf{n} . The point in the crystal has to be on the tangent plane drawn at the distance $\epsilon_{ad}v/\delta\mu$ in the direction \mathbf{n} . If this procedure is repeated for all directions \mathbf{n} , the inner envelope of all the tangent planes is the equilibrium crystal shape by construction. This procedure is called the Wulff's construction.

In Fig. 1.2 we show several possible surface energy plots, where in each panel the origin is at the geometric center of the closed curve. The planes correspond to the tangent lines. In panel a) the tangents do not re-cross the hull of ϵ_{ab} curve and the equilibrium shape coincides with the shape of ϵ_{ab} . For instance, if ϵ_{ab} were a constant, we would get a spherical droplet.

In panel b) there are \mathbf{n} directions, where the tangent runs inside the ϵ_{ab} curve. Out of these the direction where ϵ_{ab} is closest to the origin is denoted by \mathbf{n}_0 . Because all the surface points increase the total energy by an amount proportional to ϵ_{ab} at the touching point, all the surface directions outside the tangent at the direction \mathbf{n}_0 are unstable. In all these directions the shape is a plane, with normal \mathbf{n}_0 . This case is relevant for surface problems, because near a substrate the ϵ_{ab} is changed by the substrate surface energy and mutual interface energy gains, in the direction where the substrate is. This explains why the contact between the adsorbate and the substrate is usually planar.

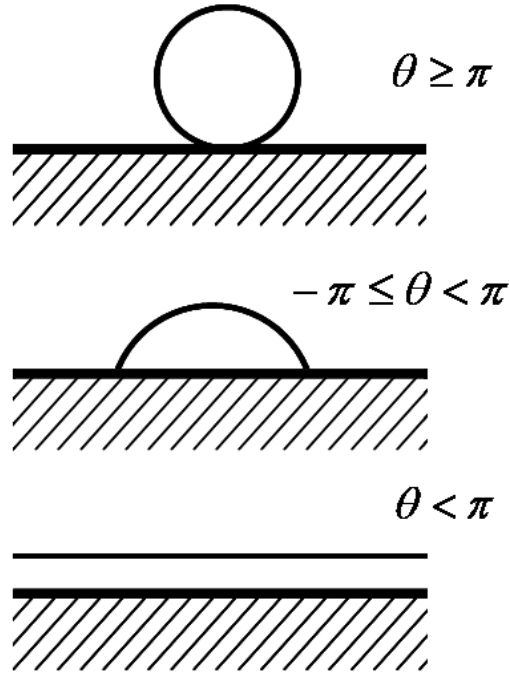


Figure 1.4: Depending on the surface energies, a liquid droplet may avoid contact with the surface, be attached to the surface or wet the surface.

The panel c) shows ϵ_{ab} for nearly perfectly faceted, free-standing crystal. If the surface energies and distances from the Wulff point for two facets i and j were $\epsilon_{ab}(i)$, $\epsilon_{ab}(j)$, r_i and r_j , the quantities would obey the relationship $\epsilon_{ab}(i)r_j = \epsilon_{ab}(j)r_i$.

In the last, final panel d) we have a surface energy from a bond counting calculation for a 2D triangular lattice. There are six sharp peaks, where the tangents are in principle undefined but by symmetry they should be perpendicular to the radius connecting the peaks to the origin. The stable shape in this case would be a hexagon. In practice the surface energies are usually known only for few low index facets but these are typically also the only ones present in the equilibrium shape.

1.4 Growth modes

Let the surface tensions between the adsorbate droplet and the vacuum and between the substrate and the vacuum be denoted by ϵ_{ad} and ϵ_{sb} , respectively, and the interface tension between the adsorbate and the substrate by ϵ_{int} , see Fig. 1.3.

In large liquid droplets the bulk structure and droplet shape are independent to a good approximation. Near the droplet corner the force balance equation $\epsilon_{ad} \int_a^b dx / \cos(\theta) =$

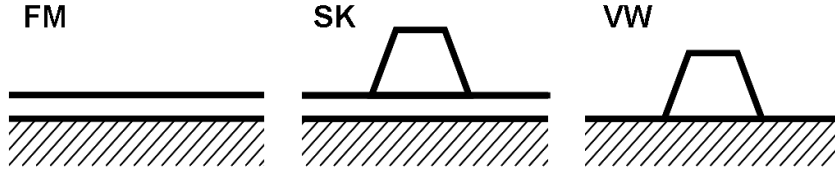


Figure 1.5: There are three growth modes, layer-by-layer or Frank-van der Merwe (FM), layer and islands Stranski-Krastanov (SK) and islands on top of a clean substrate Volmer-Weber (VW).

$(b - a)(\epsilon_{sb} - \epsilon_{int})$ turns into a condition for the so called Young's angle

$$(1.17) \quad \cos(\theta) = \frac{\epsilon_{int} - \epsilon_{sb}}{\epsilon_{ab}},$$

when the surface normal direction θ changes a little. Sometimes instead of the angle θ the angle $\pi - \theta$ is used. If the right hand side of Eq. (1.17) is larger than one, the angle θ is undefined and there are no energetic reasons for the adsorbate particle to stay in contact with the substrate. If $1 \geq \cos(\theta) \geq -1$ the particle prefers to be a segment of a sphere lying on the surface, on a facet facing the substrate. Finally, if $-1 > \cos(\theta)$ we have complete wetting, with a flat layer, see Fig. 1.4. This condition has later been modified to better describe various special systems.

In solids the lattice makes the surface energies highly anisotropic. The facets have to have low indices and therefore arbitrary contact angles are not possible.

The morphologies of the adsorbate are generally divided in three categories. When the adsorbate splits into mounds which cover only the area directly underneath them, we talk about Volmer-Weber (VW) growth mode.

The case where the surface is completely covered by a flat overlayer, is called the Frank-van der Merwe (FM) or layer-by-layer growth mode. When the deposition and the actual growth have ceased, we still refer to the morphologies with the same language, including the slightly misleading term growth mode.

When there is a collection of mounds on top of a fairly thin complete film we have the Stranski-Krastanov (SK) growth mode. The SK mode is of high importance both experimentally and technologically. Unlike the FM and VW modes, it is not addressed by the simple Young's argument presented above.

Chapter 2

Theory and methods

2.1 Molecular dynamics

Ab initio calculations are a great tool in materials modeling because the electronic degrees of freedom can be taken into account adequately and one can get quantitative results with little input information. The computational cost of ab initio methods usually increases strongly when there are more degrees of freedom and in practice one cannot perform detailed quantum mechanical calculations for systems larger than few hundreds of atoms. In computational modeling of larger systems, it is usual to resort to classical mechanics.

In molecular dynamics (MD) the center-of-mass movement of atoms is described by the Newtonian equations of motion under interatomic and external force fields. First the atomic coordinates and velocities are initialized so that the average velocity vanishes and the distribution of the speeds reflects the starting temperature. Numerical integration of the discretized equations of motion gives the time evolution of the system.

There are several ways to perform the integration. In this work we focus on the minimal energy states and paths and it is sufficient to treat both the dynamics and the thermal properties with emphasis on the computational simplicity rather than on accuracy. Therefore we use the simple leap-frog algorithm which performs decently without saving the forces,

$$(2.1) \quad \begin{aligned} \text{a)} \quad \mathbf{v}_{t/2} &= \mathbf{v}_{-t/2} + \mathbf{a}_t t; \\ \text{b)} \quad \mathbf{x}_t &= \mathbf{x}_0 + \mathbf{v}_{t/2} t, \end{aligned}$$

where t is the time step and the updates a) and b) are to be performed in alphabetical order. The algorithm can be derived by expanding the positions \mathbf{x}_t and \mathbf{x}_{-t} on the next and the previous time steps around the present position \mathbf{x}_0 as a Taylor series in the time

step t and adding the results,

$$(2.2) \quad \mathbf{x}_t + \mathbf{x}_{-t} = 2\mathbf{x}_0 + t^2\mathbf{a}_0 + 2\frac{1}{4!}t^4\mathbf{x}_0'''' + \mathcal{O}(t^6),$$

where the symbol \mathcal{O} means that the terms with equal or higher power than the argument are left out. We can further Taylor expand \mathbf{x}_{-t} and \mathbf{x}_0 around the position $\mathbf{x}_{-t/2}$ half time step $t/2$ ago and subtract the results to get

$$(2.3) \quad \mathbf{x}_0 - \mathbf{x}_{-t} = t\mathbf{v}_{-t/2} + \frac{t^3}{24}\mathbf{x}_{-t/2}''' + \mathcal{O}(t^5).$$

Inserting this into Eq. (2.2) gives the update rule

$$(2.4) \quad \mathbf{x}_t = \mathbf{x}_0 + t(\mathbf{v}_{-t/2} + t\mathbf{a}_0) + \mathcal{O}(t^3) = \mathbf{x}_0 + t\mathbf{v}_{t/2} + \mathcal{O}(t^3),$$

which shows that the accuracy of the position update rule of Eqs. (2.1) is of the third order in the time step. With similar reasoning one can show that the accuracy of the velocity update rule is of the third order.

The error of the integration shows up as a violation of the energy conservation. Typically the fast processes get integrated least accurately. This problem is usually addressed either by using a time step so small that the change in energy stays negligible for the duration of the calculation or alternatively, by keeping the velocities in the acceptable regime with a thermostat procedure.

At simplest, applying a thermostat means that the velocities get rescaled on every time step to keep the total energy constant. However, when the integration is exceptionally inaccurate, this correction cannot be done by a simple rescaling and a more elaborated method is needed. If the system studied is described by the canonical ensemble, the energy of the whole system should be able to fluctuate, with a temperature dependent variance. In the Andersen thermostat the velocities get incremented randomly, following the Gibbs distribution [26].

Another common way to modify the speeds is to use a delay which keeps the average temperature over several time steps around the correct value but leaves room for fluctuations. In the relaxation time approximation the temperature changes in time as

$$(2.5) \quad \frac{dT}{dt} = \frac{T_0 - T(t)}{\tau},$$

where τ is a time constant and T_0 is the temperature of the heat bath. If the velocities are rescaled by λ during a time step of length δt , and the kinetic energy is proportional to $k_B T$, then

$$(2.6) \quad \frac{dT}{dt} \approx \frac{(\lambda^2 - 1)T(t)}{\delta t},$$

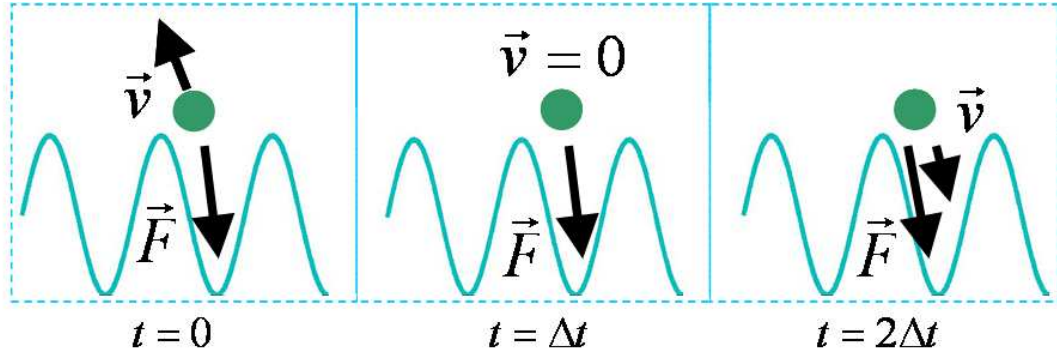


Figure 2.1: The molecular dynamics cooling (MDC) method works by cancelling the velocities every time they have a component against the total atomic force [?, 36]. On the next calculation time step the atom will then move towards the nearest local minimum.

which leads to the velocity-dependent scaling factor

$$(2.7) \quad \lambda^2 = 1 + \frac{\delta t}{\tau} \left(\frac{T_0}{T(t)} - 1 \right).$$

This is known as the Berendsen thermostat [27].

In addition to these two widely known, simple thermostats there are more accurate ways to control the temperature. As stated above, the accuracy of the thermal properties is not essential in this study. We have chosen to bring the temperature down to zero by cancelling the atomic velocities whenever they have a component pointing to the opposite direction than the total force acting on the atom. This procedure is known as the molecular dynamics cooling (MDC). The cooling is presented schematically in Fig. 2.1.

All the material parameters of MD are contained in the interatomic potentials. The forces are usually calculated from these for the integrator by another routine, which takes the coordinates as an input and returns the forces as an output. The force calculation is computationally expensive and therefore it is preferable to have as few force evaluations as possible.

It is often said that the accuracy of the atomistic methods is determined by the quality of the interaction potential. The potentials are usually phenomenological, but sometimes also ab initio calculations are employed to replace them. The potentials used in this work are discussed in the following sections.

2.2 Lennard-Jones pair potential

Among the oldest pair interaction models are Lennard-Jones (LJ) potentials, whose attractive and repulsive parts are inverse powers of the interatomic distance. The most common form has a dipole-like attraction, which can be motivated by the atomic polarizability, and a the second power of the attraction as the repulsive part, a choice which is usually made to make the potential computationally cheap.

These potentials usually have two parameters, the equilibrium distance σ and cohesive energy ϵ , and as such they are known to give decent quantitative results only for the noble gases. Their main advantage nowadays is that their application is simple and properties are fairly well-known, which makes them a good testing ground for new physical ideas.

Because the noble gas crystals are known to be very brittle, one could expect that a softer potential should give results closer to metallic systems. Ref. [28] represents a choice of the exponents and strengths of the attractive and repulsive parts which reproduces the energies of metals under various degrees of uniform compression and tension. This potential is expressed as

$$(2.8) \quad U(\mathbf{r}) = \frac{\epsilon}{m-n} \left[n \left(\frac{\sigma}{r} \right)^m - m \left(\frac{\sigma}{r} \right)^n \right],$$

where ϵ is the bond energy, σ the equilibrium distance, $r^2 = \mathbf{r}^2$ and $m = 8, n = 5$ are exponents which give the interaction the metallic, soft character. For Pd, $\sigma = 2.75 \text{ \AA}$ and $\epsilon = 3.91 \text{ eV}$.

When $r_a < r < r_c$, where r_c is the largest radius for considering two atoms as neighbors and r_a is the lower cut-off radius, we multiply $U(\mathbf{r})$ of Eq. (2.8) with a smooth cut-off function $\theta(\mathbf{r})$,

$$(2.9) \quad \theta(\mathbf{r}) = 3 \left(\frac{r_c - r}{r_c - r_a} \right)^2 - 2 \left(\frac{r_c - r}{r_c - r_a} \right)^3,$$

following Zhen *et al.* [28].

At $r = \sigma$ the potential reaches its minimum, $-\epsilon$. The curvature $\partial_r^2 U$ at the minimum is $nm\epsilon/\sigma^2$, which is related to the bulk modulus B at the zero temperature,

$$(2.10) \quad B = -V \left(\frac{\partial p}{\partial V} \right) = \frac{1}{9\sigma} \left. \frac{\partial^2 U(r)}{\partial r^2} \right|_{r=\sigma}.$$

The Eq. 2.10 gives $B = 130 \text{ GPa}$ for Pd. The experimental value is around 180 GPa which is still of the right order of magnitude and sufficiently accurate for our qualitative studies.

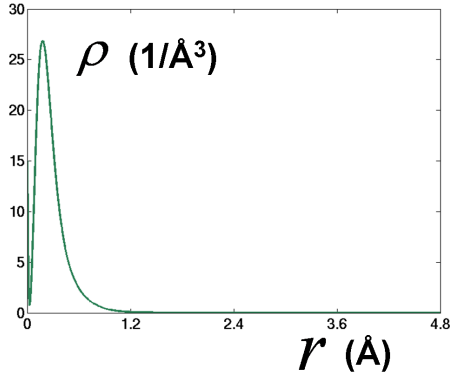


Figure 2.2: Electronic number density as a function of the distance.

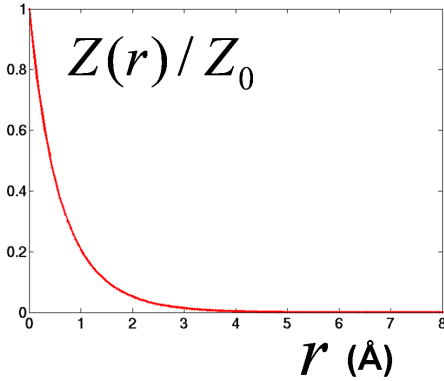


Figure 2.3: The positive nuclear charge is shadowed by the surrounding electrons, an effect which is described by the effective charge Z .

In tests of Ref. [28] the potential was found to be in agreement with Embedded Atom Method (EAM) calculations. We also compared the compressibility curves for this LJ parametrization with corresponding EAM results and the match was very good for Pd and slightly less so with Cu. The Embedded Atom Method is discussed in section 2.3.

We introduce the misfit between the substrate and adsorbate by setting the adsorbate lattice constant to a value which differs by 100*f* % from the substrate lattice constant,

$$(2.11) \quad f = \frac{a_{\text{ad}} - a_{\text{sb}}}{a_{\text{sb}}}.$$

The equilibrium bond length between substrate and adsorbate particles is set to the arithmetic mean of the respective lattice constants.

Analogously with the misfit we introduce an interaction parameter

$$(2.12) \quad \kappa = \frac{\epsilon_{\text{int}} - \epsilon_{\text{sb}}}{\epsilon_{\text{sb}}} = \frac{\epsilon_{\text{ab}}}{\epsilon_{\text{sb}}} \cos(\theta),$$

which is used to set the depth of the substrate-adsorbate potential and which is related to the interfacial tension. When the interaction parameter is positive (negative), the substrate-adsorbate contact becomes more (less) expensive.

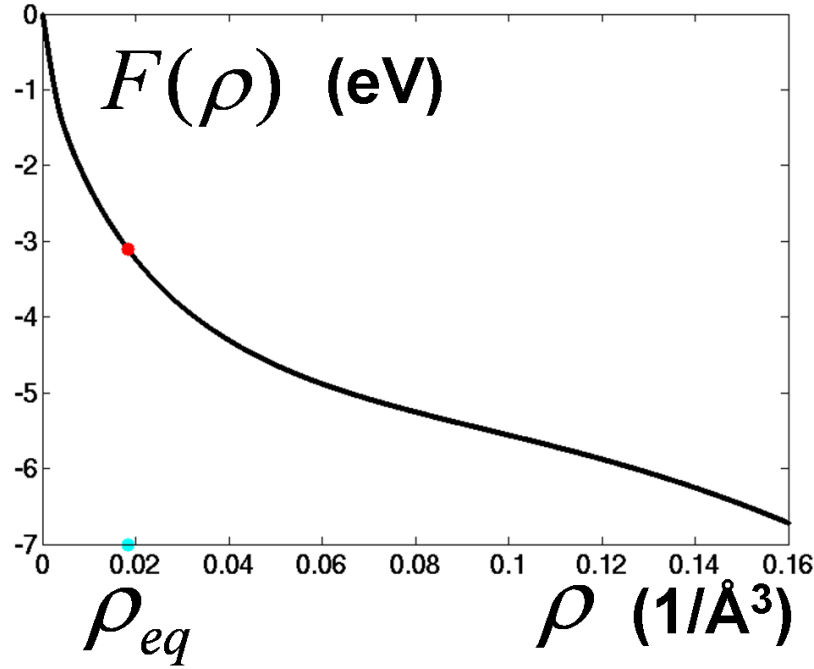


Figure 2.4: The embedding energy decreases as the surrounding electronic density increases. The equilibrium embedding energy is shown as a dot on the curve.

2.3 Embedded Atom Method

The elastic properties of metals cannot be described accurately with any pair potential. It can be shown that for any pair potential $V(r)$

$$(2.13) \quad \omega^2(001) = \frac{1}{2} [\omega^2(110) - \omega^2(1\bar{1}0)] + k^2 \frac{1}{r} \frac{\partial V(r)}{\partial r},$$

where $\omega(abc)$ is the angular frequency of a phonon on fcc lattice propagating in direction (abc) with wavevector \mathbf{k} . On the other hand, from the wave equation for lattice vibrations

$$(2.14) \quad \begin{cases} \omega^2(110) - \omega^2(1\bar{1}0) &= \frac{v}{m} (c_{12} + c_{44}) k^2; \\ \omega^2(001) &= \frac{v}{m} c_{44} k^2, \end{cases}$$

where v and m are the atomic volume and mass, and c_{11} , c_{12} and c_{44} are elastic constants. When the virial theorem holds,

$$(2.15) \quad \frac{1}{r} \frac{\partial V(r)}{\partial r} = 0.$$

which means that the elastic constants satisfy the Cauchy relation $c_{12} = c_{44}$.

It is well known that for most metals this Cauchy relation does not hold. For palladium $c_{11} \approx 234.1$ GPa, $c_{12} \approx 176.1$ GPa, and $c_{44} \approx 71.2$ GPa [29]. In Embedded Atom Method (EAM) this problem has been fixed by splitting the interaction into an attractive embedding potential F and to a repulsive pair potential [30, 31]. One can think that an atom in the solid is an impurity and the rest of the solid is a host. By Hohenberg-Kohn theorem the energy of the unperturbed host is only a function of the electronic density and the energy of the impurity is dependent on the location of the type and location of the impurity. Thus, it can be argued that the energy functional also should be dependent on these three factors,

$$(2.16) \quad E = \sum_{i=1}^N V_i(\rho(r_i), \nabla\rho(r_i), \dots).$$

The cohesive energy of a solid is related to the width of the local density of states contributing to the metallic bonding. We take the local density of states at atom i to be proportional to the sum of electronic densities ρ_j from the neighbour atoms j . With ionic repulsion due to the cores, one can write the following energy functional

$$(2.17) \quad V_{\text{eam}}(i) = F_i\left(\sum_{i \neq j} \rho_j(r_{ij})\right) + \sum_{i \neq j} U_{ij}(r_{ij}),$$

for the atom i . Here F_i and U_{ij} are the attractive and repulsive energy contributions, and $r_{ij} = |\mathbf{r}_i - \mathbf{r}_j|$ is the distance between atoms i and j .

Even though the electronic density functions ρ_j are spherical double gamma functions, as presented in Fig. 2.2, we can distinguish between fcc and hcp crystals because they have the same numbers of atoms on the first and second neighbor shells but differ at the third neighbor shell.

The shape of F_i as a function of the electronic density is shown in Fig. 2.4. It is similar to shape of the related Finnis-Sinclair embedding energy which is just the negative square root of the density [32]. Heuristically, the embedding function can be thought to describe how the energy of an electronic gas changes when a solid is formed by bringing in positively charged atomic cores from infinity.

The core repulsion term

$$(2.18) \quad U_{ij}(r_{ij}) = \sum_{j \neq i} \frac{Z_i(r_{ij})Z_j(r_{ij})}{r_{ij}}.$$

The form of this term is motivated by a Coulomb repulsion where the screened, effective charge Z_i depends on the distance to the atomic core, see Fig. 2.3. The subscript i reminds that the effective charge is screened differently for each atom type.

The total energy of EAM potential under uniform compression and extension is shown in Fig. 2.4. There are many different variants of EAM potentials. The variant we are using is the original parametrization [30, 31]. It has been tested thoroughly in numerous studies and also shown good agreement with the experiments on Cu/Pd(001) system [33]. Although we are not considering systems which mix, it needs to be mentioned that this EAM variant does not predict the right structure for the bulk alloys of the same materials [34].

2.4 Activation-minimization procedure

The so called activation-minimization procedure finds some of the strain relaxation structures of stressed islands and overlayers basically in three steps. First, we choose an initial state which can be assumed to be a few defects away from some realistic low-energy state.

The initial state is usually obtained by minimizing the energy of a pseudomorphic structure, where the adsorbate has the equilibrium lattice constant of the substrate. A more detailed descriptions of the initial states for islands and overlayers are given in sections 3.2 and 4.3, respectively.

Second, the locally minimized initial state undergoes an activation treatment, which helps the system to cross energetic barriers. The activation treatment consists of "tilting" and subsequent MDC under repulsive bias potential (RBP), see section 2.5 and Refs. [35, 36, 37]. By tilting we mean changing the transition probabilities away from of the initial

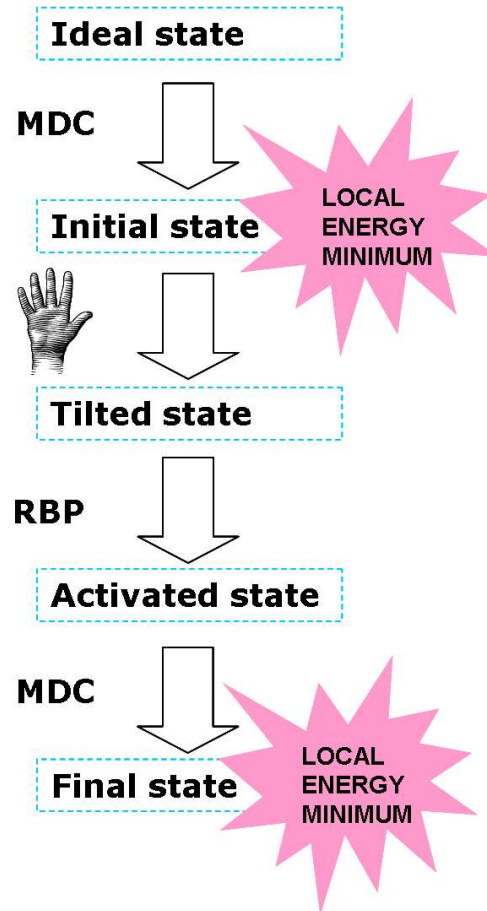


Figure 2.5: The activation-minimization procedure starts by relaxing a pseudomorphic state, "tilting" the transition probabilities by a small disturbance and letting the system to seek a new local minimum under a repulsive bias potential (RBP) (see section 2.5.) During RBP we save a few intermediate states. Finally, the new state is energy minimized without the bias.

state by pushing some selected atoms closer to an edge of the local potential minimum where the atom is located. More details on this are also provided in subsection 2.5. It should be noted that tilting is not used in Publications 3 and 5.

During the activation we save a chain of intermediate states to be used as an input for the energy barrier finding method described below and in section 2.6. After the activation treatment we perform one more MDC without the RBP to make sure that the system has evolved to a different local energy minimum. All the steps of the activation-minimization procedure are summarized in Fig. 2.5.

To find the transition paths, saddle points and energy barriers for the processes we get from the activation procedure, we use the Nudged Elastic Band method (NEB) [38] on the chain of intermediate states saved during the activation. The minimal energy path contributes the highest weight to the transition probability between the initial and final states and it gives the dominant defect nucleation mechanism at low temperatures. In brief, the NEB method minimizes the energies of the chain of transition states and at the same time keeps the chain continuous. A more detailed description of NEB method is given in section 2.6.

2.5 Repulsive Bias Potential

Before applying the Repulsive Bias Potential (RBP) we "tilt" the transition probability towards a direction which is likely to initiate a nucleation process. This is done to increase the chance of getting certain kind of defects. In practice the tilting is performed simply by altering the coordinates of some selected atoms. Depending on the sign of the lattice mismatch, the push is better to be done upwards with compressive misfit and downwards with tensile misfit. A sideways push is useful in both cases. Sometimes the disturbance of individual atoms or of small compact planar clusters does not lead to stable dislocations and in these cases we may push whole close-packed rows in the bottom adsorbate layer. In Fig. 2.6 the tilting would be represented by a left or right shift in the location of the system state in the potential landscape.

In the Repulsive Bias Potential method the atoms experience a non-local, repulsive external potential [35, 36, 37]. The new potential energy surface is written as

$$(2.19) \quad U_R(\mathbf{x}_1, \dots, \mathbf{x}_N) = \sum_{i < j}^N V(\mathbf{x}_i - \mathbf{x}_j) + A \exp\left(-\sum_{i=1}^N (\mathbf{x}_i - \mathbf{x}_i(0))^2 / R^2\right),$$

where A and R represent the amplitude and the spatial decay constant of the repulsion potential, $\mathbf{x}_i(0)$ is the coordinate of particle i in the initial state and N is the number of particles. If the bias has short range, the barrier energies stay unaffected. The bias amplitude decreases when the deviation from the initial configuration becomes larger.

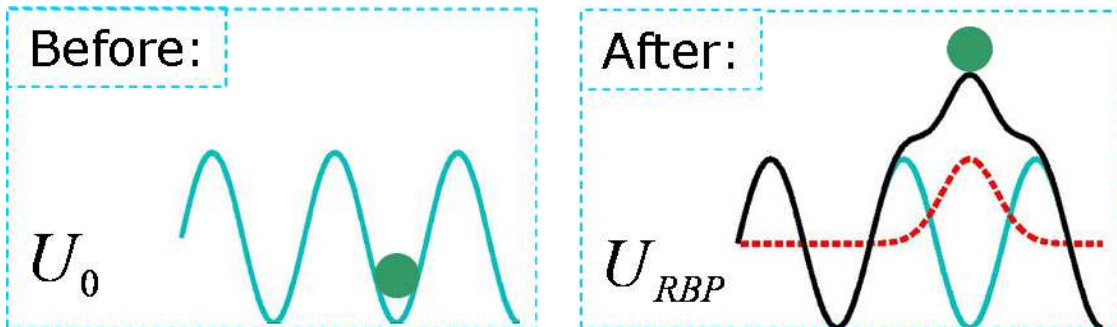


Figure 2.6: Repulsive bias potential (RBP). The bias makes any local minimum in the configuration space unstable. The additional term decreases if any of the coordinates deviates from the initial value.

After the initial tilting, we push the system to a new local minimum with RBP. This trick prevents the system from returning to the initial state and lowers the escape barriers to other states.

We found that the repulsive bias works efficiently, when most of the substrate is kept frozen. Because there are usually more ways to realize the same release of bias potential with several particles than with a single particle works in favor of the multi-particle processes. When a large volume of substrate is allowed to be mobile during the activation, the small displacements of this domain add up and release a fraction of the bias potential. To prevent this, only the topmost substrate layer is free to move when RBP is applied. Below the mobile layer we have two layers of immobile atoms and so the total substrate thickness on this stage can be as low as three layers.

When we have used an unrealistically thin substrate during the activation, we correct it later by adding six more layers under the original system before continuing with the NEB method. During NEB, all the transition states are minimized again with thick substrate and thus our final energy values take into account the substrate relaxation effects.

It is important to note that the RBP method can generate many different final states depending on both the initial displacements used for the activation, and the exact form of the repulsive bias. However, our results were checked by varying the simulation cell size and levels of biasing and our conclusions are not dependent on these details.

2.6 Nudged Elastic Band-method

Nudged Elastic Band method (NEB) is a way to find minimal energy paths in complicated configuration spaces. The method is introduced in great detail in Ref. [38] whose presentation this section closely follows. For N particles the configuration space is $3N$

dimensional. In zero temperature the greatest contribution to the transition probability between two states comes from the minimal potential energy path.

As an input NEB needs a chain of coordinate sets, or "images", which describe a transition of the system from an initial state to a final state. Often this chain is parametrized by a "reaction coordinate" s which measures the progress of the transition and is often proportional to the $3N$ -coordinate distances from the initial to the final state.

It is necessary that there are more images than there are extremal points on the transition path. If the shortest distance between two extrema along the path were s_e and the total length of the transition path s_t , then according to the sampling theorem a safe number of equally spaced images would be $\geq 2s_t/s_e$. In practice s_e is difficult to estimate accurately before doing the calculation but adjusting the number of images by trial and error works in most cases.

The minimal energy path cannot be found simply by minimizing the energies of each image individually, because this would drag them all to the nearest local minima and leave no information about the energy barriers behind. One cure for this is to add an artificial harmonic potential

$$(2.20) \quad V(\mathbf{x}(0), \mathbf{x}(t)) = \frac{k}{2} [|\mathbf{x}(t) - \mathbf{x}(0)| - a]^2,$$

between the images at successive sampling time steps 0 and t . Here \mathbf{x}_t denotes a $3N$ dimensional vector containing all the coordinates on time step t . The parameter k is an arbitrary spring constant and a is some suitable value of the distance between two images

$$(2.21) \quad |\mathbf{x}(t) - \mathbf{x}(0)| = \sqrt{\sum_{i=1}^N [\mathbf{r}_i(t) - \mathbf{r}_i(0)]^2}.$$

Imposing the potential of Eq. (2.21) between the images is equivalent to forcing the continuity requirement with a Lagrangean multiplier. This method is sometimes called the plain elastic band (PEB) method.

The problem with the PEB method is that if the guess for the equilibrium distance a is too large the path will begin to meander like a real elastic band when it is under compression along its length. If the equilibrium distance is too small, the images will start to cluster. The nudged elastic band (NEB) method is developed to fix this issue.

In NEB the force between the images is split into components parallel and perpendicular to the path. The clustering is caused by the parallel component and therefore, if it is projected out, the equilibrium image distance can be set to any small value or to zero. However, this kind of artificial harmonic potential would become identically zero if the successive images were at right angles,

$$(2.22) \quad \mathbf{r}_1(t) \cdot \mathbf{r}_1(0) + \mathbf{r}_2(t) \cdot \mathbf{r}_2(0) + \dots + \mathbf{r}_N(t) \cdot \mathbf{r}_N(0) \equiv |\mathbf{x}(t)||\mathbf{x}(0)| \cos(\theta(t, 0)) = 0.$$

Especially when the transition path bends strongly, the likelihood of cutting corners grows.

To prevent this, the parallel component can be gradually turned back on with a switching function $f(\theta)$. The idea behind this is that if the path curves strongly, more images get pulled to the corner to make the sampling there more accurate. A popular choice for $f(\theta)$ is $\cos^2(\pi \cos(\theta)/2)$.

2.7 Phase Field Crystal model

For comparison purposes it is useful to have another independent method to do the same calculations. The Phase Field Crystal (PFC) method has been shown to reproduce the essential features of a large variety of solid state systems where elasticity plays a role [39]. Its main advantage over the molecular dynamics methodology is that it yields results in diffusive time scales while the spatial resolution remains atomistic.

In PFC model we take a free energy functional

$$(2.23) \quad F[\rho] = \int dV \left\{ \frac{1}{2} \rho [r + (q^2 + \nabla^2)^2] \rho + \frac{1}{4} \rho^4 + h\rho \right\},$$

where ρ is the number density, q is the k -vector of the shortest vibrations, h is an external potential and r is a temperature control parameter. This form of the free energy can be derived by truncating the free energy of the density functional theory of freezing which in turn is derived for the gas phase [40, 41, 42]. For liquid and solid phases this functional can be considered to be an extrapolation.

Like in section 1.3, the stationary densities correspond to constant chemical potentials, $\mu = \delta F / \delta \rho$. If the chemical potential is not constant, there has to be an atom flux \mathbf{j} towards the lower potential, $\mathbf{j} = -\nabla \mu$. With a constant total number of atoms we get the evolution equation

$$(2.24) \quad \frac{\partial \rho}{\partial t} = \nabla^2 \mu.$$

Usually we add a noise term on the right side to speed up the iterative solution of ρ .

In our overlayer studies in Publication 2 we take the phase field to represent the adsorbate. The substrate is described by an external pinning potential

$$(2.25) \quad h(x, z) = h_0 (\cos(kx) \cos(kz/\sqrt{3}) - \cos(2kz/\sqrt{3})/2),$$

which is nonzero only when $2z \leq 3\pi\sqrt{3}/k$. The pinning potential wave length k is chosen to respect the boundary conditions of the simulation cell and the pinning potential strength is related to the interface energy between the substrate and the adsorbate. More

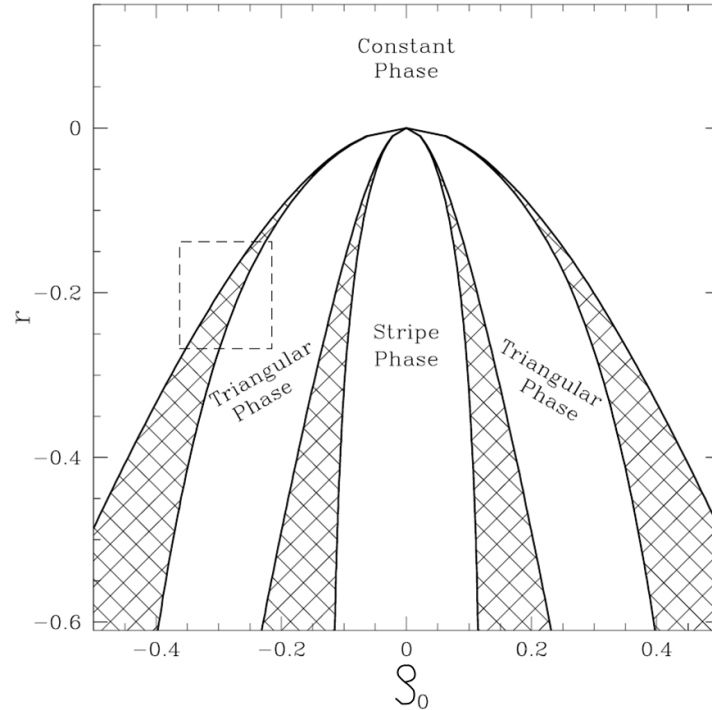


Figure 2.7: The 2D phase diagram of the PFC model from Ref. [39]. The horizontal axis is the average value of the phase field (density) and the vertical axis is the control parameter r (temperature). The different areas denote the parameter regions where various periodic solutions are stable. The dark areas correspond to coexistence regions and the values inside the square box represent a typical choice for an overlayer system.

details are given in Publication 2. The lattice mismatched wave number q of the adsorbate is then set equal to $k/(1 + f/100)$.

In the solid phase ρ is periodic in the diffusive time scales, and in the gas or liquid phase ρ is smooth on the same level of time-like coarse-graining. If we have a solid and another phase in the same volume, we need to find parameters which correspond to a coexistence region of these two possible solutions of Eq. 2.24. The choice of the parameters is done with the aid of 2D phase diagram of the PFC model, which is reprinted in Fig. 2.7 from Ref. [39]. The parameter r is related to the temperature of the simulation. The physical meaning of the average phase field ρ_0 is related to the average density or to the average amount of solid in the simulation cell. By setting the r and the simulation cell size in values which are in the coexistence region, for instance inside the rectangular box of Fig. 2.7, we have found a description for a system where a known coverage of adsorbate interacts with the substrate from Eq. 2.25.

Chapter 3

Results: Islands

3.1 Heteroepitaxial stress release and islands

As the Wulff's construction in section 1.3 verifies, the islands can be a part of the ground state even when the lattice constants of the substrate and the adsorbate would agree. A peculiarity of the heteroepitaxial systems is that the stress can de-stabilize a flat film and be the crucial factor determining the growth mode.

The balance between the stress and surface energies is often delicate. In nanoscale the surface effects are strong and the effective elastic constants and surface tensions may differ from their continuum limit values [43, 44]. There are several possible stress release mechanisms ranging from undulation, buckling [12, 45] and dislocations [46] to island [12, 14, 20, 47, 48, 49, 50, 51, 53, 54] and nanowire [55, 56] formation and mixing [57]. We are only considering cases where mixing plays no role.

In Publications 1-4 we study the island stress release pathway. As explained in the introduction, our model is two dimensional. Our technique is very similar to the approach used by Thibault *et al.* [58] and Uemura *et al.* [59].

In principle it is possible that the number of islands per unit area is set by their mutual, repulsive elastic dipole interactions [13, 20, 55], mediated by the relaxation in

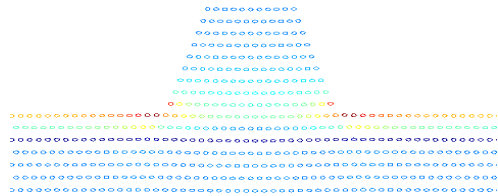


Figure 3.1: The atomic potential energy (from Eqs. (2.8) or (2.17)) has its maxima at the ends of island's bottom layer. The surface layers are removed from the image to improve the contrast of the bulk energy distribution. The lowest energies are found from the substrate-adsorbate interface.

the substrate and the wetting film. In this study we are not considering this situation. Whether or not this has been seen experimentally has been under debate because it is difficult to distinguish a true equilibrium state from a persistent metastable, kinetically trapped state, which is separated from the true equilibrium by a large energy barrier.

When the heteroepitaxial stress release is used to generate surface structures, the growth is stopped at a low coverage. From this starting point the overlayer gradually develops towards the equilibrium state, often slowly. We are considering the case where the equilibrium state consists of islands and the island density is determined by the early nucleation stages. On this stage there is usually not enough material to form a continuous film. This kind of process has also been considered by several authors [15, 49, 50, 51].

In our calculations the condition of fixed island density is realized by the fixed unit cell size l_w , which in principle determines the number of islands per unit area. However, because our islands are weakly interacting, the simulations can also be interpreted to describe the immediate surroundings of an isolated island. In this case the actual coverage cannot be known precisely, except that it must be below the value corresponding to a perfectly periodic arrangement. In this interpretation our results have relevance for a variety of nominal coverages with weakly interacting islands.

After the nucleation stage the islands grow at the expense of the wetting layers. When compared to a flat layer, an island always introduces new surface area with an associated energy cost. However, if the strain in the film is large enough, the mound formation can lead to lower total energy. In Publications 1, 3 and

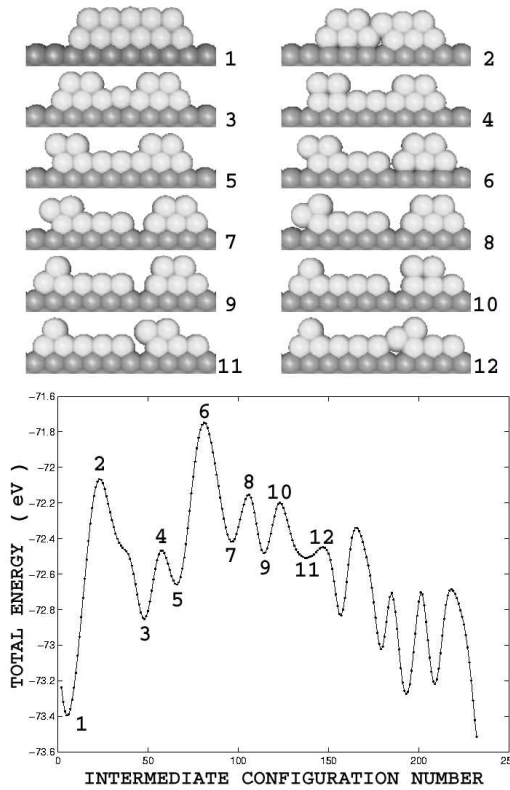


Figure 3.2: One realization of the decay of an 11-atom arrangement goes through a complicated set of intermediate states. First the island creates a small partial dislocation by glide mechanism. Part of the island sinks down to the center of the bottom layer, a process similar to the incorporation in the context of overlayers, see section 4.4. After these steps the rest of the atoms in the second layer diffuse to the edges of the bottom layer and fall to the substrate-adsorbate interface. The calculation was done with RBP activation and the transition path was minimized with NEB method. The resulting energy landscape and barriers are shown in the lower panel.

4 we have constrained the islands to grow coherently with the substrate. As a result, at a certain size the dislocation nucleation barrier must vanish. The coherent growth is related to the early growth and in the continuum limit the majority of the bulk stress has to be released by defects.

When the islands grow at the expense of the wetting film, one can talk about “thinning energy” on a coarse grained level [50, 51]. The thinning energy decreases strongly as a film gets thicker. For instance, with long range interactions the thinning energy could be related to the direct interaction of the substrate with the second, third and more distant adsorbate layers. Any volume removed from the island is a thinning energy gain, but on the other hand islands relax more efficiently leading to a stress energy gain proportional to the island volume. Because the former contribution is decreasing while the latter is increasing, it is possible that there is a volume where the terms balance each other [49, 51, 50]. We study this question more closely in Publication 3 and give more details in section 3.6.

3.2 Two-dimensional islands

Our island results in Publications 1-4 are two-dimensional. This choice can be motivated for instance by continuum elasticity, where it is conventional to look at cross-sections of beams as 2D objects. From the practical point of view this allows us to test and compare a large number of island geometries in a feasible computer time.

In our initial state we always have a number of complete substrate layers and an adsorbate structure which is entirely pseudomorphic. In Publication 1 we consider all the possible concave island shapes without overhangs, keyholes and which are reflection symmetric about a line perpendicular to the substrate surface. It should be noted that while there are indications that overhang formation may take place when small metallic islands assemble on oxide surfaces, in metal-on-metal systems this is unlikely [52]. In Publications 3 and 4 we are restricted to islands where the number of atoms in successive layers can only differ by three. In these cases the island and the wetting film we can have a partial wetting film width is limited only by the simulation cell width.

One way to write down all the island configurations with only steep facets and a partial wetting film underneath, is to first subtract the wetting film contribution from the total amount of adsorbate particles. The maximal height for an island is that of an equilateral triangle. If the maximal height $h = (\sqrt{4N - 1} - 1)/2$ is an integer, it corresponds to an acceptable island configuration, otherwise one can take the largest integer less than this value as a trial starting height. For all the heights smaller than this one can work out a formula which gives the corresponding l_w and test whether it is an integer, or just simply test whether the correct particle number can be obtained with any l_w between the given

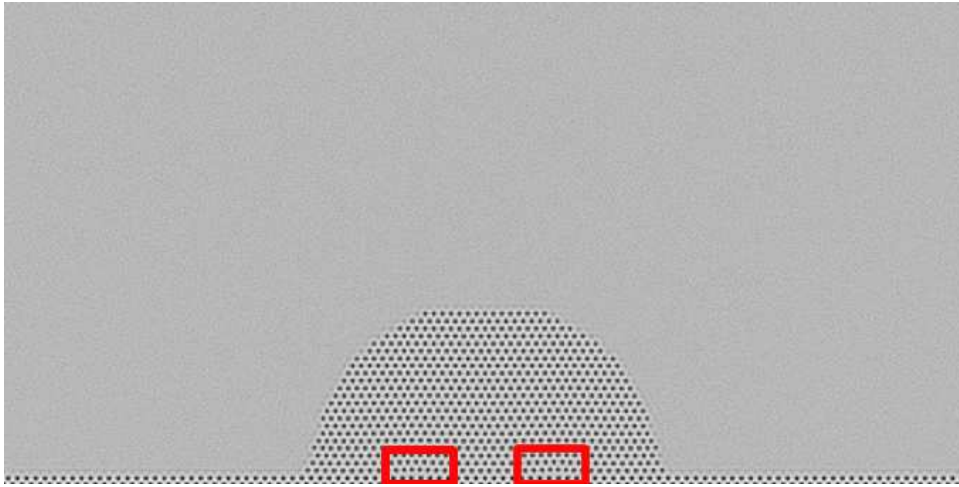


Figure 3.3: The PFC simulations show how a pair of dislocations is nucleated at the bottom edges of an island. The dislocations move close to the center of the bottom layer. In this work we study primarily the case where the islands remain coherent with the substrate. The calculations of Publication 2 show that in both atomistic and phase field modeling the nucleation process has a finite energy barrier. The substrate pinning potential is described by the Eq. (2.25) in section 2.7 (reprinted from Publication 2.)

height and the maximal width, like we did. The maximal width is the smaller out of the simulation cell width and the available adsorbate particle number.

The partial wetting film configurations can be included in two ways. If we first subtract the prescribed number of atoms in the partial wetting film from the total number of atoms and then write down the island configurations as above, the partial wetting film atoms can be added between the wetting film and the island in the end. An alternative way to get the same result is to subtract the difference between the island base width the partial wetting film width from the total number of atoms, then write down the islands as before and add the subtraction to the bottom island layer. For a given amount of adsorbate, the plausible partial wetting film sizes are between the base width of an equilateral island and the simulation cell width.

If we want to find all the possible configurations without overhangs or holes, we can proceed by splitting the available particle number into a smaller and a larger part and applying the same steps to the smaller part until all the possibilities are exhausted. Out of these one can select for instance only the islands which don't have known high-energy facets, or those which are mirror symmetric about a line perpendicular to the substrate surface. This process could also be used to find the partial wetting film configurations. In the end we have a list of particle numbers in successive layers for every possible island satisfying our conditions.

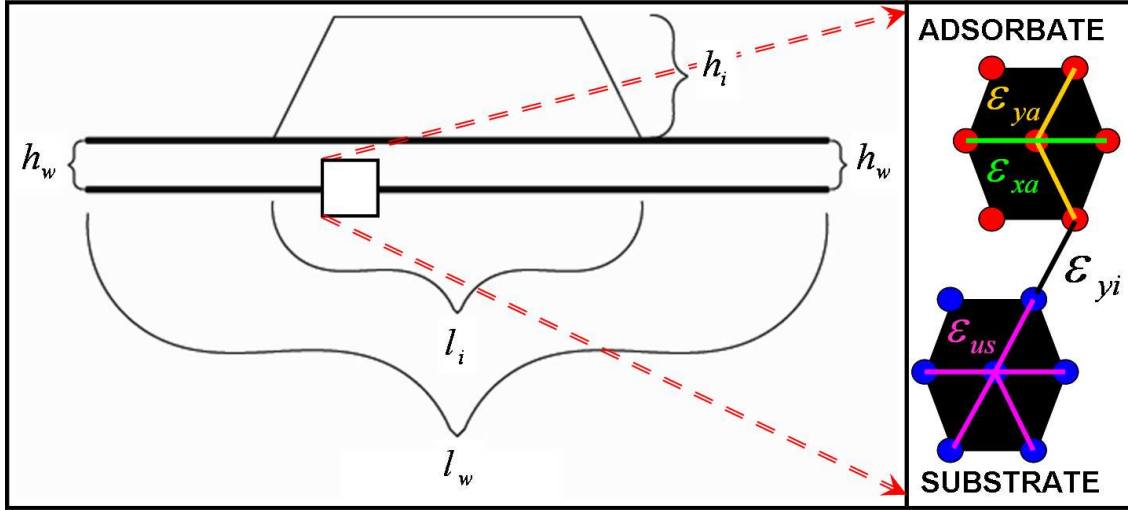


Figure 3.4: The heights h_\diamond and widths l_\diamond of an island and a wetting film have $\diamond = i, w$ respectively. In an ideal, unrelaxed pseudomorphic system there are only few different bond energies. The energies of horizontal and diagonal adsorbate bonds are denoted by ϵ_{xa} and ϵ_{ya} , the bonds between the adsorbate and the substrate have energy ϵ_{yi} and all the substrate bond energies are equal to ϵ_{us} .

3.3 Island shapes at low coverage

In Publications 1, 3 and 4 we study the equilibrium shapes of 2D nanoislands. We write down all the plausible pseudomorphic shapes with a fixed N , as described in section 3.2, and relax them with Molecular Dynamics Cooling, see section 2.1 for details. During the minimization the system releases stress energy and the displacement field becomes non-uniform. Among the configurations the equilibrium shape is the one that has the lowest energy.

It is hard to find the ground state directly by applying a minimization scheme to an arbitrary initial state because typically the energy landscapes between the growth modes are rugged. A sample minimal energy transition from a coherent 11-atom island to the flat ground state is shown in Fig. 3.2. Even in this case the landscape shows a complicated structure with large energy barriers between the multiple local energy minima.

We find the equilibrium shapes for range of coverages, measured by the deposited amount of adsorbate N and for a range of f . The results of Publication 1 indicate the preferred growth mode for each pair of N and f when $\kappa = 0$. We repeat the same calculation for positive, and negative values of the interaction parameter κ with a low total coverage in Publication 3. In the parameter range we use in our studies we see no plastic deformation and the islands remained coherent with the substrate.

When the parameter κ is positive, the islands prefer the VW growth mode. With negative κ the adsorbate prefers to be flat when the misfit f is small. At a certain value of f the flat layer becomes unstable and the preferred growth mode changes to VW. The transition lines between various modes are not symmetric in the tensile and compressive cases. This is partly related to the asymmetry of the potential, partly to the geometric differences, like the fact that unlike the compressive stress, the tensile stress cannot be released by undulation. All the found ground states belong either to FM or to VW growth mode.

The basic island shape we find is a truncated pyramid, see Fig. 3.1. At most one additional facet is found. This facet is located either between the top horizontal facet and the side facets or at the island bottom, between the substrate and the side facets. On few occasions the extra facet split the side facets into two halves. This rare case was related to high f and N where our method is least reliable. At least it could be seen as an indication that the fourth most common island shape might belong to this category. These results compare well with those of Ref. [60].

With larger island sizes corresponding to coverages above three complete atomic layers we see nucleation of dislocations from the bottom corners of the island. To initiate a nucleation process, we activate a large faceted island without tilting as explained in section 2.5. This is in agreement with other studies on the subject [61, 62]. For comparison purposes we also make the same calculation with PFC model, as shown in Fig. 3.3. The generic features of the process in the PFC model are in line with the MD results. See Publication 2 for more details.

3.4 Island relaxation and energy

To study how the stress energy is released in islands, we select a representative set of islands with the same height but with varying width. We relaxed all the configurations and plotted the deviation of the atomic potential energy from the energy of an ideal pseudomorphic system as a function of the atom location. The plot is shown in Fig. 3.6.

The stress relaxation is different depending on the aspect ratio and volume of the island. When the island width is large in comparison to the height, the stress becomes localized near the steep walls and the bulk of the island is stressed. In narrow islands the relaxed zones are overlapping and the bulk of the island is unstrained. This corresponds to the steep parts of relaxation energy gain curves in Fig. 3.6. Because the relaxed region near the island walls has its own characteristic width, the bulk of the island is relaxed only when this characteristic width is of the order of the island diameter. For larger islands this effect disappears. This corresponds to the regime where the curves of Fig. 3.6 tend to constant values.








	$-6\epsilon_{us}N_S$
	$-(2\epsilon_{xa} + 4\epsilon_{ya})N_A$
	$-2\epsilon_{us}(l_w - l_i - l_0)$
	$2\epsilon_{ya}l_0$
	$2(\epsilon_{ya} + \epsilon_{xa})h_i$
	$2\epsilon_{ya}(l_i - h_i)$
	$(2\epsilon_{us} + 2\epsilon_{ya} - 4\epsilon_{yi})(l_0 + l_i)$

Figure 3.5: Each surface in the reference system has an associated energy penalty or gain which can be calculated by counting bonds. The dark areas in the cartoon on the left denote the part of the system which is described by the corresponding expression on the right side. The quantity $l_0 = (l_w - l_i)\delta_{h_w,0}$.

The actual minimal energy islands are always between these two extremes, and the competing contributions come from the surface energy cost of the island walls, which favors low aspect ratio and from the relaxation energy gain, which favors high aspect ratio.

In an ideal pseudomorphic system there are only a few different bonds, see Figs. 3.4 and 3.5. In Fig. 3.5 we partition the energy into bulk and surface contributions. Using the geometrical parameters and bond energies from Fig. 3.4 we can calculate a reference total energy for any ideal pseudomorphic system. The relaxation energy gain Ω of our calculations is the difference of the reference total energy and the energy after the minimization of the system energy, as shown in Fig. 3.6.

In the regime of flat, wide islands the relaxation energy gain saturates. The maximal gain or the value of relaxation energy gain Ω in the flat part of Fig. 3.6 is fitted by

$$(3.1) \quad E_{\text{shallow}} = -0.194(7)h_i(h_i + 8.16(7))\epsilon_{us}.$$

With this, the gain Ω for height h_i is

$$(3.2) \quad \Omega = E_{\text{shallow}} - b \left[l_i - l_c - \sqrt{(l_i - l_c)^2 + d^2} \right].$$

By fitting Ω for data sets with different fixed values of h_i the height dependence of b, l_c

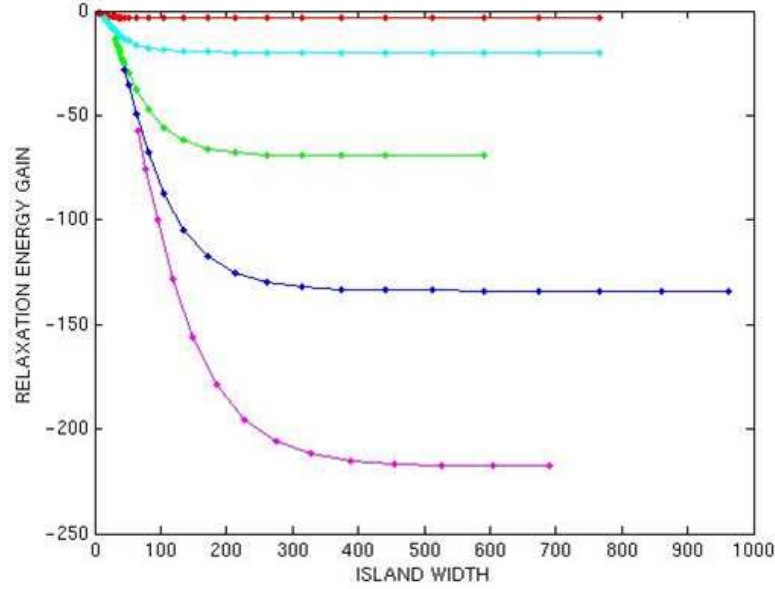


Figure 3.6: The difference Ω between the numerically calculated total energy and the analytical reference energy for a pseudomorphic configuration reaches a constant value when the island width is large. In this limit the relaxation energies associated with the steep island facets move farther apart independently as the island width is increased. The fixed heights for the curves are 5, 15, 31, 45 and 59, from up to down. The agreement between Eq. 3.2 and the data is good.

and d is seen to be

$$(3.3) \quad \begin{cases} b = 0.0134(2)h_i(h_i + 1.602(2)); \\ l_c = 2.45(7)h_i + 8.47(3); \\ d = 1.21(0)h_i + 8.82(0). \end{cases}$$

The calculation of Ω for various island aspect ratios and different misfits f revealed that the f -dependence of Ω is well described by simple, shape-independent scaling with f^2 . This is what one would expect from linear elasticity. For instance, if one considers the island corners as edge dislocations with horizontal Burgers vectors $fl_i/2$, this scaling comes out of Eq. 4.1. The κ -dependence was orders of magnitude too small to affect our results.

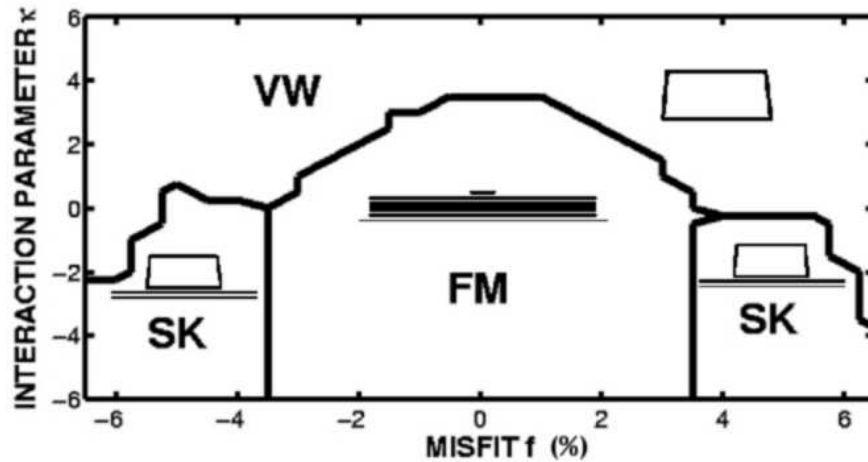


Figure 3.7: The growth mode depends both on the mechanical stress and on the strength of the bonds between the substrate and adsorbate. The former is parametrized by the misfit f (horizontal axis) and the latter by interaction parameter κ (vertical axis). When the contact angle between the substrate and the adsorbate is negative and the misfit is not too large, wetting occurs. For small f we have complete wetting and the FM growth mode and for large f or positive κ the adsorbate prefers the VW mode. The SK mode is seen with negative κ and intermediate values of f (reprinted from Publications 3 and 4).

3.5 Global phase diagram

In Publication 1 the deposited amount of adsorbate is low and we do not find the SK growth mode, as described in section 3.3. In higher coverage regime the number of shapes which satisfy the constraints explained in section 3.2 becomes very large. However, because all the found minimal energy shapes in the low coverage regime belonged to the class of truncated pyramids with a maximum of one pair of high energy facets, we restrict our high coverage calculations to the three most common shapes, described at the end of section 3.3. Because the optimal shapes require exchange of material with the wetting film, we include at most one partial wetting film of arbitrary width between the island and the complete layers.

Both the mechanical stress and the potential depth at the interface are important for the SK mode. In Publications 3 and 4 we study the interdependence of these two factors by mapping the growth modes systematically for various combinations of the respective interaction potential properties. We call this map the "global phase diagram" (GPD). The result is presented in Fig. 3.7. Again there is a clear difference between the tensile and compressive strain.

All the three growth modes appear in the GPD of Fig. 3.7. The boundary between

the VW and other modes is curved. Most of the positive κ territory is in VW and it appears that with a sufficiently large misfit the growth mode becomes VW even with negative κ . The FM mode is near the $f = 0$ axis on negative κ side and its boundary with the SK mode seems to be relatively independent of the misfit. As the misfit f increases, the island shape becomes higher and sharper. Our conclusions continue to hold for larger coverages but for the smaller coverages the phase boundary between the FM and SK becomes blurred. Our GPD is in agreement with the similar results of Ref. [63]. The minimization with Eq. 3.2 is capable of reproducing the Fig. 3.7 even though the fitting was done just in one point of the same figure.

3.6 Optimal island shape and size

The optimal shape question cannot be answered without varying the coverage. From the GPD we learned the parameters which favor the SK mode. By fixing the values of f and κ to the SK regime we can vary the coverage to see how the island geometry depends on the coverage.

The results are presented in Figs. 3.8 and 3.9. When there is not enough adsorbate to cover the whole substrate surface, the overlayer is a planar film which gradually expands in width. Above the coverage of precisely one monolayer, there is a clear transition from the FM mode to the SK mode. The island is in the truncated pyramid shape and it is ambiguous whether there is a partial wetting film or a pair of high-energy facets at the bottom of the island.

According to our results, the partial wetting film is not a very effective buffer against island shape variations. Both the island width and height increase with coverage but there is a certain wiggle on top of the monotonous increase, which is caused by the partial wetting film increasing while the island shape does not change. This difference between the predictions of Eq. (3.2) and our direct simulation is related to the corner energies which were deliberately neglected. Our results thus support the viewpoint that the optimal size is dependent on the coverage [49, 51, 50].

In a very narrow region of coverage this kind of wiggle indeed could be interpreted as a kind of optimal shape mechanism present in this model. Because the possible island shapes are not a continuum in the low coverage limit, for some numbers of deposited atoms there are sizeable gaps between the successive, realizable aspect ratios. If after addition of one atom it is impossible to find an island, which obeys the symmetry constraints and whose aspect ratio is close enough to the optimum, the additional atoms get dumped to the partial wetting film. As mentioned above, this threshold depends on the corner energies which are not included in Eq. (3.2). Thus, to some extent this kind of optimal shape mechanism is based on the configuration space limitations.

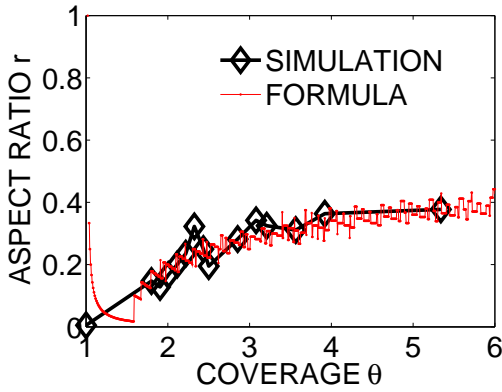


Figure 3.8: The curve without marker shows the minimal energy island aspect ratio as a function of the coverage and the markers present the aspect ratios for the same set of islands where the energy minimization is done using Eq. (3.2). In Publications 3 and 4 this minimization was done analytically with the same formula. The agreement between the direct simulations and the predictions of the formula is good.

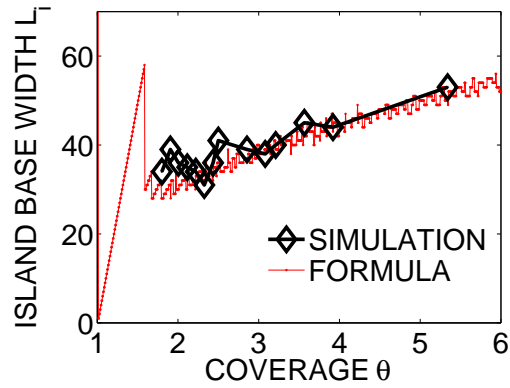


Figure 3.9: The markers show the bottom layer widths for minimal energy islands as obtained from the direct simulation and the continuous curve is the prediction of Eq. (3.2), as in Fig. 3.8. The agreement is again good. In Publications 3 and 4 the formula was minimized analytically.

3.7 Comparison of 2D and 3D results

In Publications 1,3 and 4 we mention that our 2D approach is applicable to 3D systems as well. Our results already agree with the 3D island results of Refs. [50, 51] and the generalization of our methodology to 3D structures is straightforward. However, the comparison of the actual 2D and 3D results can be done most directly with nanowires. In this section we shall look at the global phase diagram for nanowires.

We chose the surface to be studied to be the close-packed fcc(111) surface. The cross-sections of the wires studied had 820 row ends, see Fig. 3.11. The shapes of the cross-sections were variations of the slightly skew truncated pyramid shape, without overhangs, keyholes or other imperfections which would make the wire not simply connected or not monotonous. We generate the cross-sections like described in section 3.2.

The allowed shapes have either one of two rows ends missing from the top pyramic layer or one or two additional row ends in the layer just above the first continuous film under the pyramid. The resulting number of shapes in this case was just 57. The width of the system in the direction of the nanowire was eight atomic spacings. The substrate thickness is six layers.

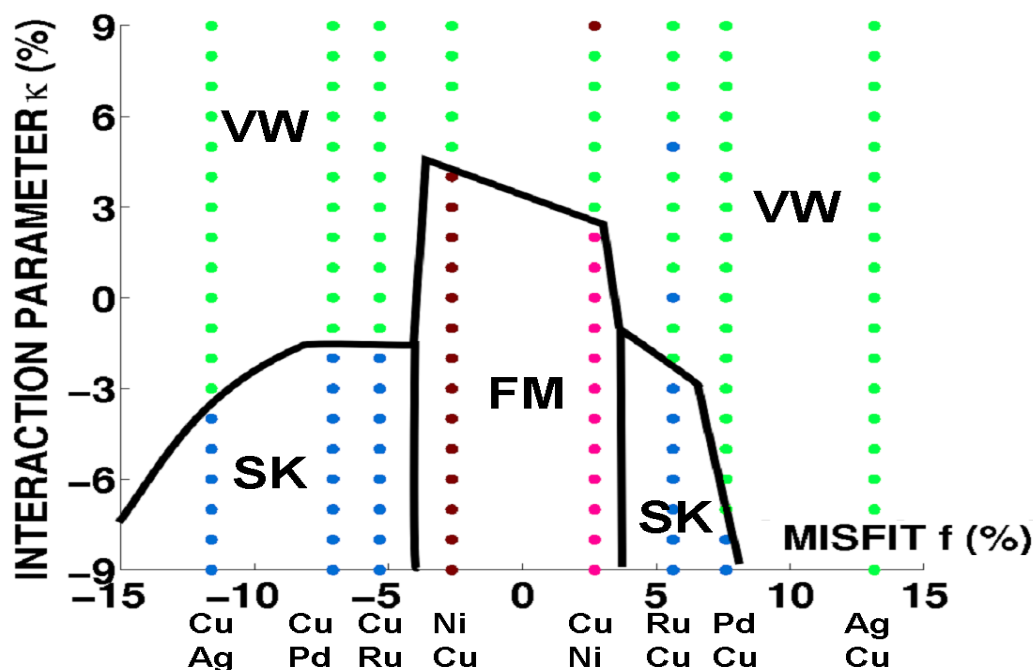


Figure 3.10: The 3D and 2D global phase diagrams are qualitatively similar. The former was calculated for ridges on fcc(111) surfaces for pairs of materials listed below the horizontal f axis. The upper and lower materials are the adsorbate and the substrate, respectively. The lightly colored domain has VW islands, the left and right "wings" have one layer of wetting film and more than 9 layers thick island and the slice in the middle consists of four or three wetting films and one or two layers thick islands. An example of a high island is given in Fig. 3.11.

In Fig. 3.10 we have plotted the wetting film thickness as a function of the misfit f and the interaction parameter κ . The misfits correspond to the values of the bimetallic pairs in Table 3.1. It has to be pointed out that only a few pairs in the Table 3.1 are stable against mixing. Furthermore we do not expect our LJ interactions described in section 2.2 to give more than qualitative trends.

The dark lines which separate various growth modes are drawn as guides to the eye. In the VW mode there is no wetting film. We have combined the four and three layers thick wetting films to the FM mode, although in both cases there is a flat island on top of the film (heights one or two layers, respectively.) In SK mode the wetting film thickness is one and the island height above nine layers. See Fig. 3.12 for illustration.

The general characteristics of the phase diagram in Fig. 3.10 are the same as in the 2D case, see Fig. 3.7. The main difference to the 2D case is the abundance of dislocations, see Fig. 3.12. In 2D the small islands remained coherent with the substrate up to fairly

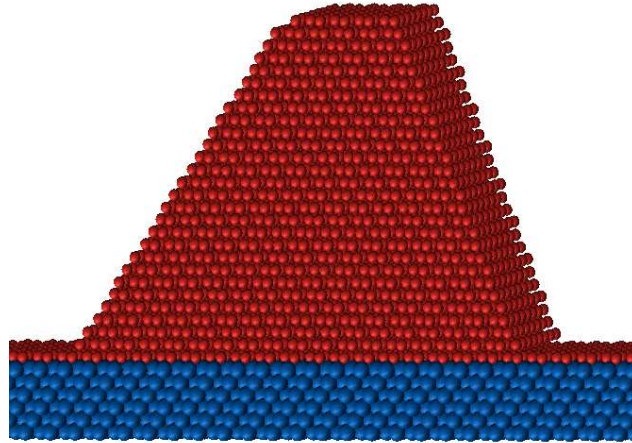


Figure 3.11: An eight atomic spacings thick section of a nanowire on fcc(111) surface. In this geometry the left and right slopes are different. In the side view the slopes correspond to a triangle whose bottom edge is of length 3 and the other edges are of length $2\sqrt{5}$ and $\sqrt{17}$. Ultimately the asymmetry between the left and right slopes is a consequence of the period three stacking sequence of fcc(111) planes. See Fig. 4.1 for illustration.

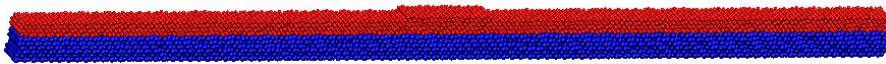
large misfits, but in 3D the structures with an identical 2D cross-section would generate defects with much less strain. To create an edge dislocation, one has to move the atoms over a site of potential energy maximum in 2D but in 3D one has enough geometric freedom to go around the maximum site, see also Fig. 4.2 for a similar process. In this sense the difference is as can be expected.

The potential energy released by the dislocations affects strongly the aspect ratio of the nanowire. While in 2D the island height increased with the misfit, in 3D the height always jumped down when a new dislocation arrangement was introduced. Because higher islands cost more surface energy, this effect is also consistent with our 2D results.

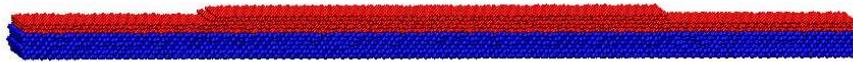
Table 3.1: Misfit (%) and mixing in 300 K for selected bimetallic pairs

Substrate	Adsorbate	Misfit	Alloying	Reference
Ag	Cu	-11.6	No	[64]
Pd	Cu	-7.07	No	[25]
Ru	Cu	-5.33	No	[65]
Cu	Ni	-2.63	Yes	[66]
Ni	Cu	2.70	Yes	[66]
Cu	Ru	5.63	No	[65]
Cu	Pd	7.61	Yes	[25]
Cu	Ag	13.1	No	[64]

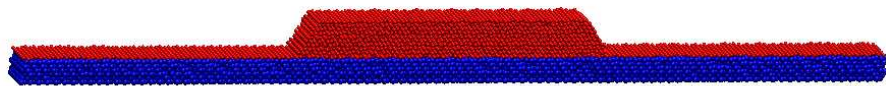
FM: $f < 0$



FM: $f > 0$



SK



VW

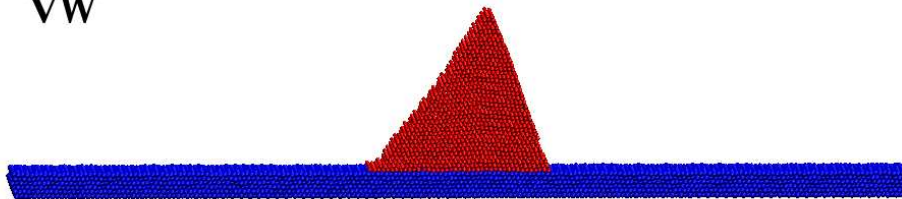


Figure 3.12: The nanowires can be classified to growth modes in terms of the wetting film thickness. The minimum energy shape of the FM mode with misfit $f < 0$ in Fig. 3.10 is shown in the first panel from the top. For $f > 0$ the FM shape is shown in the second panel. Since the configuration on top of the complete layers is actually two layers thick, the shape could also be classified to be in the SK mode. The third panel from the top shows the minimum energy SK nanowire with the smallest $f > 0$. The last panel illustrates one of the VW nanowires. Note the abundance of dislocations inside the structure.

Chapter 4

Results: Overlayers

4.1 Dislocations and the fcc(111) surface

Face centered cubic (fcc) and hexagonal close-packing (hcp) lattices have the highest packing efficiency $\pi/\sqrt{18}$ that can be achieved with spheres of equal radius. Fcc has the same numbers of atoms on the first and second neighbor shells as the hcp lattice. Both lattices can be thought to be made out of planes where the atomic nuclei are at the corners of equilateral triangles, as shown in the first panel of Fig. 4.1. These are called the $\{111\}$ planes of fcc and $\{0001\}$ planes of the hcp lattice.

An identical layer can be placed on top of the first close-packed layer in two ways. The difference between the fcc- and hcp-lattices comes from the placement of the second plane which can be either start a new sequence or use the second alternative, resulting in periods of two or three, respectively. This is illustrated in the second and third panel of Fig. 4.1. If only the two topmost layers are taken into account, the atomic arrangement of hcp(0001) is indistinguishable from fcc(111) and both surfaces can be expected to have the same generic features.

In a perfect lattice all the atom locations are connected by lattice vectors and the sum of all vectors forming a closed loop vanishes. If the lattice is distorted, it may be possible to find closed loops along the approximate atom-to-atom lattice vectors whose sum does not vanish. The sum of the lattice vectors along the loop defines a Burgers vector \mathbf{b} associated with the defect which goes through the loop.

Generally the most common dislocations are the edge and screw dislocations. If a cylinder is cut open along a radial half-plane, an edge dislocation is obtained by moving the other wall of the cut radially by \mathbf{b} , while a screw dislocation is formed by pulling the wall \mathbf{b} along the cylinder axis again by \mathbf{b} , before sealing the cut. This is known as the Volterra construction. The cylinder axis is often known as the dislocation line. For the

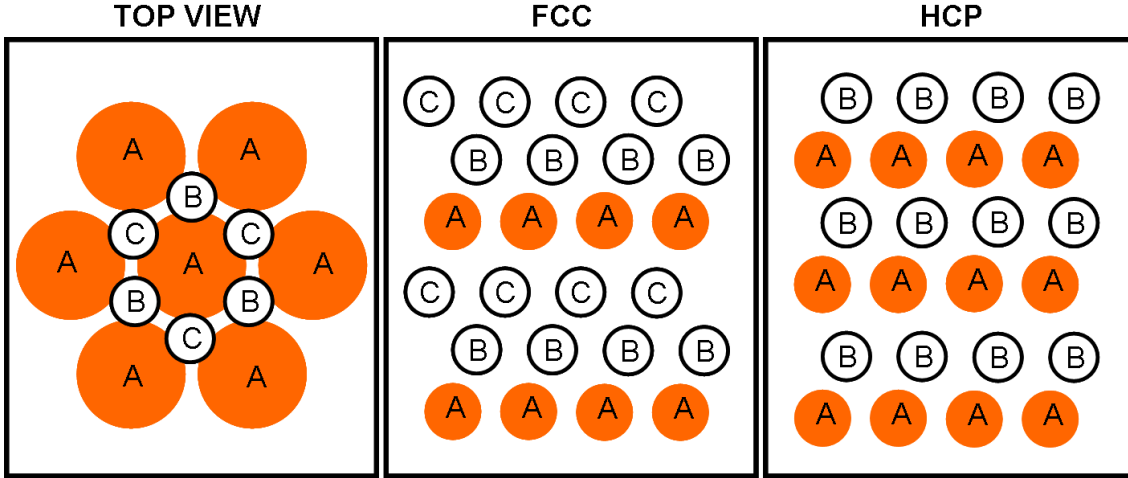


Figure 4.1: On fcc(111) surface each layer has potential minima in a honeycomb pattern.

edge dislocation the Burgers vector is perpendicular to the dislocation line.

The line energy density of an edge dislocation is

$$(4.1) \quad w(\mathbf{b}) = \frac{\mu b^2}{4\pi(1-\nu)} \log\left(\frac{R}{a}\right),$$

where μ is the shear modulus, a is the radius of the dislocation core and R is the distance from the dislocation line to the surface. As a function of the Burgers vector size, the energy is an upwards bending curve. Consequently, by the principle of energy minimization, when anisotropy is weak and core energy can be omitted, dislocations with large \mathbf{b} generally prefer to split into several dislocations with shorter values of \mathbf{b} . This is called the Frank's rule.

A stacking fault is a planar dislocation, where \mathbf{b} atomic layers are added or removed from the stacking sequence. Its Burgers vector is normal to the plane. Bulk stacking faults are energetically more expensive than line dislocations but on surface they do not cost more than edge dislocation loops. Because fcc(111) surface has two alternative sites with nearly identical energy stacking faults are formed easily [67, 68].

4.2 Shockley partials and stacking domains

A partial dislocation is such that its the Burgers vector length is only a fraction of a full lattice vector. A Shockley partial is partial edge dislocation whose Burgers vectors is symmetry equivalent to $(112)/6$ [67, 68]. The Shockley partials are common in fcc-crystals.

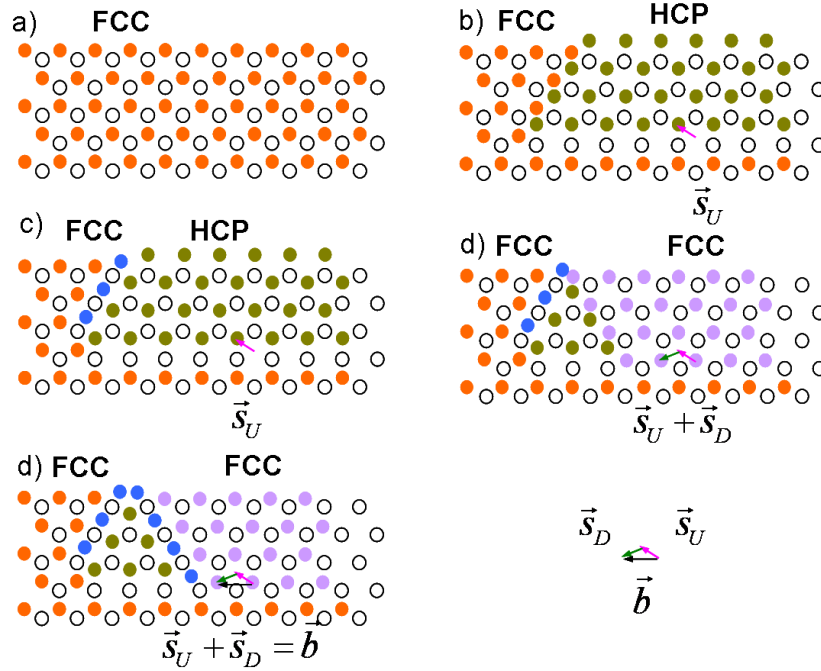


Figure 4.2: Overlayer can release tensile stress by increasing its density. By first moving a domain by \vec{s}_U and then by \vec{s}_D , as shown in the panels b) and c), one can create an edge dislocation \vec{b} as in panel c) and d). If the edge dislocation is filled with adatoms, we get an HCP domain bounded by heavy and superheavy walls. Another dislocation must be created at the same time to cancel the net movement of the overlayer. The panel d) shows the relaxation of a domain wall to bridge sites, as in the superheavy configuration. In an inverse order the panels would describe how an edge dislocation \vec{b} on fcc(111) surface splits into two Shockley partials.

In Fig. 4.2 we show how a stacking domain can be formed. Instead of directly moving a domain by one lattice vector, one first pushes the domain on the hcp-sites and then splits it in two parts which return to the original or different fcc-sites. These domains cannot be fitted together with perfect dislocations. Instead, the domain boundaries can be recognized as Shockley partials.

Because hcp-layers could also be obtained by skipping one layer in the correct fcc stacking sequence, the fcc and hcp domains can also be seen as surface stacking faults. From this point of view the Burgers vector for the corresponding planar dislocation would have a component perpendicular to the surface. In this work we view the domain boundaries only as line dislocations and correspondingly we consider only the Burgers vector components which are along the surface, as shown in Fig. 4.2.

Creation of dislocations is expensive energetically and therefore to a good approx-

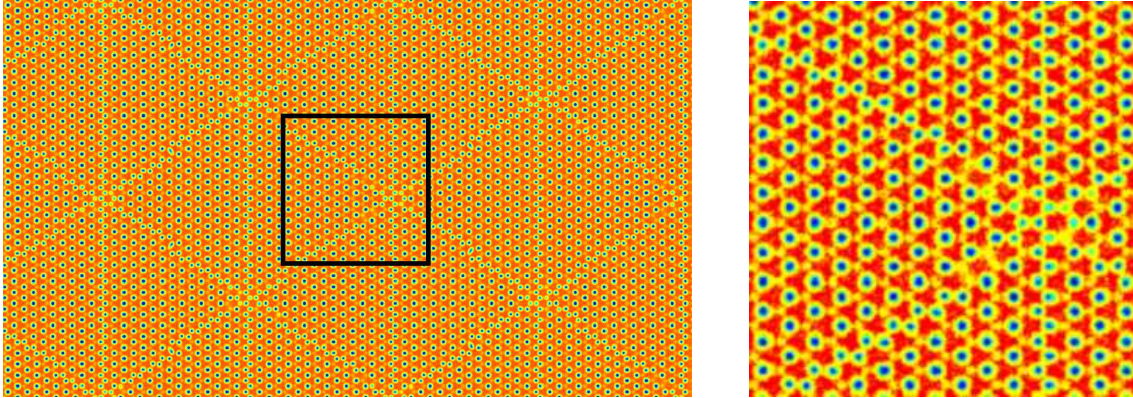


Figure 4.3: Phase Field Crystal adsorbate produces stable fcc and hcp domains on weak honeycomb lattice of potential wells. The substrate in this case is $\text{MIN}(0, 0.9h_0 - h(x, z)) + \text{MIN}(0, 0.9h_0 - h(x, z + a/\sqrt{3}))$ where $h(x, z)$ is given by Eq. (2.25), a is the distance between maxima of h and MIN returns the smaller of its two arguments. The vertical axis is measured by the coordinate x and the horizontal by z . The area surrounded by the dark line is shown in the right panel. The alternative stacking sites are visible as light spots between the dark number density maxima. The contrast of the image has been improved to show both sites.

imation it has been observed that the Burgers vectors are conserved in decay reactions, $\mathbf{b}_{i+j} = \mathbf{b}_i + \mathbf{b}_j$, see Fig. 4.2. On the fcc(111) surface, by Frank's rule any edge dislocation with Burgers vector equivalent to $(110)/2$ splits into two Shockley partials.

There are several kinds of domain walls. One variant has atoms at bridge positions and in the other variant the atoms in different domains are facing each other. By analogy to the commensurate-incommensurate transition, the domain walls can be classified into heavy, superheavy, light and superlight [69].

This classification depends on which material one takes as the reference. If the domain wall geometry is compared to the substrate, the walls are heavy, because the adsorbate number density prefers to exceed that of the substrate. We call the bridge site domain wall as a superheavy wall, because it resembles the corresponding bridge site configuration in incommensurate-incommensurate transition literature, although its density is lower than that of the other wall type. If we would have used the adsorbate as a reference, the both domain boundaries should have been called light walls.

In a larger scale the domain-like structures on the fcc(111) surface also follow the hexagonal symmetry. As patterns the domains are zig-zag lines [70] or triangles [71]. In Fig. 4.3 we show a result of a PFC calculation, where a 2D phase field adsorbate relaxed on an external honeycomb substrate (see Fig. 4.1) whose misfit was -5.5% . This value of misfit corresponds to Cu/Ru(0001) surface where such patterns have been observed with direct imaging [72, 73, 74, 75, 76]. This alternative method also revealed splitting into

stacking domains with hexagonal symmetry. The domain walls in the PFC model appear to be different, which is probably due to the different treatment of the core repulsion between the particles.

The reason for the zig-zag patterns becomes more apparent if one builds an island or a wire out of the same material, like the one in Fig. 3.11. The opposite sides of a line are not equivalent. As a result, for a one layer thick straight ribbon there would be a force that would pull the structure in one direction or the other, which is why a stable ribbon has to wiggle to cancel the net force.

4.3 Pseudomorphic overlayers

In our overlayer studies the Pd(111) substrate and Cu adsorbate layers are fitted to a rectangular simulation box. The material in the initial state consists of close-packed layers stacked so that the every three layers the atomic positions match in the direction vertical to the layers. The simulation cell is chosen to have one edge aligned with an in-layer close packed row and one edge normal to the layer. We refer to the latter as the vertical direction. Periodic boundary conditions are applied across the horizontal simulation cell edges. Because of this, our results can be interpreted as weakly interacting periodic surface structures.

The two bottom substrate layers are fixed to their initial ideal locations which is justified when the substrate is very thick. Each substrate layer can be viewed as a collection of equilateral triangles. We select the total number of these triangle edges to accommodate a single row dislocation. The number of atomic rows in the longer horizontal direction is then chosen to be twice that of the shorter horizontal direction. Because periodic boundary conditions are used, this box choice allows the close packed diagonal rows along the triangle edges to be continuous over the box boundaries. With the lattice parameters of Cu/Pd(111) this settles the minimal simulation cell size to $15a_s \times (15a_s\sqrt{3})$, where a_s is the lattice parameter of the substrate. The edge atom numbers along the simulation box boundaries are 15 and 30.

4.4 Stacking domains and incorporation

To study the stress relaxation of overlayers, we first looked at complete overlayers in the same fashion as we studied the islands. When the initial state is only one layer thick, eight atoms out of 512 are pushed to the surface and the adsorbate splits into fcc-hcp stacking domains. The process takes place without barrier. The removed adatoms are typically in few clusters near the left-behind vacancies whose mutual locations are not

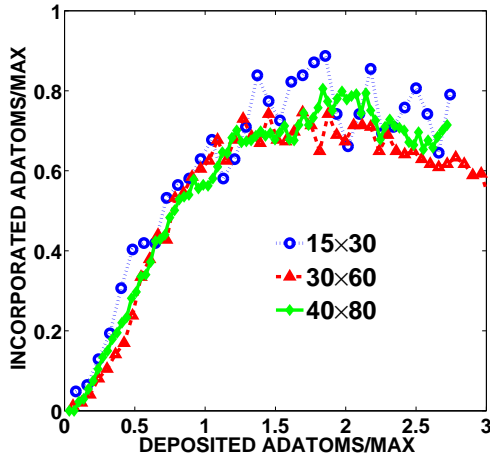


Figure 4.4: The number of adatoms which get incorporated into the bottom adsorbate layer first increases linearly with the number of adatoms which were initially placed on top of complete pseudomorphic film. The number of adatoms needed to release the tensile stress completely, denoted by MAX, is approximately $2f \times$ the layer size. The curves calculated for three different layer sizes agree when both axes are scaled with the corresponding MAX.

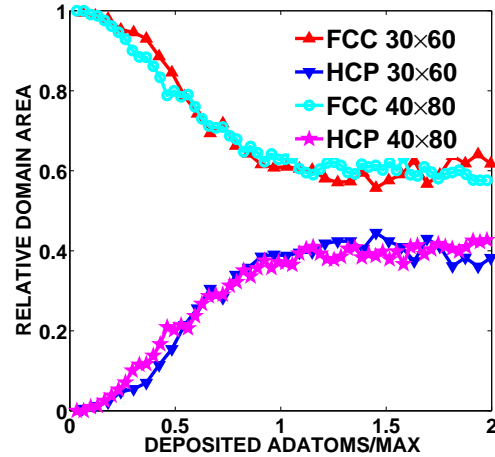


Figure 4.5: After incorporation the initially pseudomorphic adsorbate layer closest to the substrate splits into fcc and hcp stacking domains whose relative areas are estimated with diagrams like in Fig. 4.6. Most atoms stay in the original stacking. The vertical axis is the number of atoms in each stacking, normalized by the layer size, and the horizontal axis is as in Fig. 4.4. The results for two layer sizes agree with this scaling. Only the atoms originally in the pseudomorphic layer are taken into account.

clearly correlated. We discuss the multilayers more thoroughly in section 4.6.

To see what happens when the coverage does not correspond precisely to a complete substrate layer, we proceed by placing a few adatoms at randomly selected locations on top of the full adsorbate layer. Both the complete adsorbate overlayer and the adatoms follow fcc stacking of the substrate. After the minimization we see that some adatoms have become incorporated into the layer below them.

The upper panels of Fig. 4.7 show the patterns corresponding to fcc and hcp stackings. The images were made by leaving out the top substrate layer because in hcp the second-to-top layer coincides with the first adsorbate layer while in the fcc it doesn't. The large figure shows the curved, fairly irregular pattern of domains. The barrier for the formation of the domains with the adatom incorporation process was

too small to resolve. While our results indicate that such domains are expected to form, we cannot say much about their mutual organization because our simulation cell size was of the same order as the domain size we see. We used the activation-minimization technique with heavy tilting to find transition paths from the fully pseudomorphic complete monolayer to a dislocated layer with fcc and hcp domains. According to the calculations the highest energy barriers are of the order of 1 eV.

As described in Publication 5, we use Basin-Hopping global optimization method [77, 78] with the same EAM potential as described in section 2.3 to study how small platelets in the submonolayer regime relax. We saw that after a certain critical size, the minimal energy clusters also split into stacking domains thereby supporting our activation-minimization results.

The number of atoms which get incorporated is shown in Fig. 4.4, where out of the adatoms initially placed on the surface (horizontal axis) the number indicated by the vertical axis is eventually found from the layer of adsorbate facing the substrate (vertical axis). To compare the results for calculations with different simulation cell sizes, both axes are normalized with the amount of atoms needed to completely relieve the strain (MAX). For each simulation cell size this is roughly $2f$ times the number of atoms in a single substrate layer. Fig. 4.4 indicates that with this scaling the incorporation takes place similarly for any simulation cell size.

Fig. 4.5 shows rough estimates of the numbers of atoms in the fcc and hcp stackings. To make the estimate, the atoms from the complete adsorbate layer of the initial state have been classified according to their final state displacements. In the two alternative stackings each atom is located above the center of an equilateral atom triangle of the layer below. The distribution of the displacements is approximately bimodal, see the sample in Fig. 4.6. The first maximum

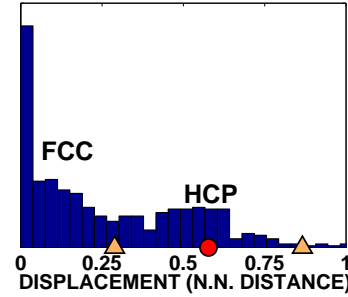


Figure 4.6: Some atoms in the substrate-adsorbate interface move to the nearest hcp site. The hcp displacements are between the triangular markers.

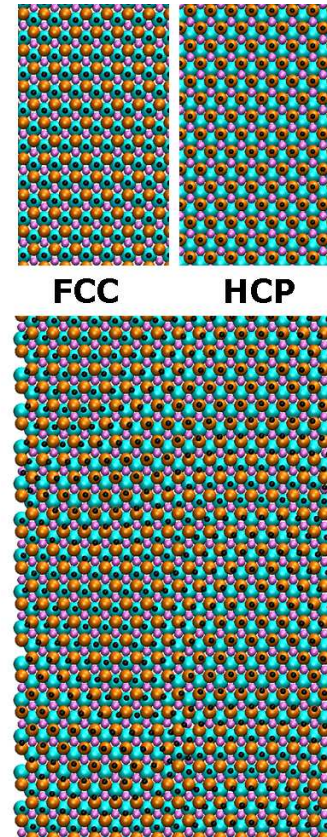


Figure 4.7: The adsorbate forms fcc and hcp stacking domains.

is located at zero and the second around $u = a_f/\sqrt{3}\text{\AA}$, which corresponds to the center of a neighbor triangle. The shortest distance to the edge of the triangle is $u/2$. Thus, if the displacement is found to be inside this distance from the first peak, it is classified to be in the fcc phase and if it is inside the same distance from the second peak, it is counted to be in the hcp phase. This procedure leaves some fraction of the material unclassified and does not classify atoms at high energy locations correctly, but nevertheless it shows the same trends that can be seen directly from visualizations such as Fig. 4.7.

4.5 Comparison to experimental findings

In Publication 5 we discuss the relation of our findings to the existing experimental data. We did not find any direct imaging data on ultrathin Cu/Pd(111) films but several authors had studied the relaxation with diffraction and spectroscopic methods [23, 24, 25, 79]. According to the measurements there was no mixing below temperature 450 K. From the RHEED peak intensities it was inferred that the Pd like lattice constant dominates below coverages 3-4 ML and after that the lattice constant goes to the relaxed value of Cu [25]. Although there is speculation about the possible presence of dislocations, the interpretation of the peaks was that the growth stays epitaxial up to the critical coverage above 3 ML.

According to our results the dislocations do appear already in the submonolayer regime. To estimate their effect on the average lattice constant we calculated the average structure factor for eight realizations of the incorporated single layers the along the direction corresponding to the horizontal axis of Fig. 4.7. The structure factor is shown in Fig. 4.8. Because both the fcc and hcp domains are nearly pseudomorphic, they contribute to the Pd-like peak. The Cu-like peak comes from the domain boundaries. Because there is more than one kind of domain boundary, the Cu peak appears to be split. Thus, our results are not in contradiction with the experimental data.

The structure factor of Fig. 4.8 suggests that when the stress is released by the domain boundary mechanism below the critical coverage, the average lattice constant will stay close to substrate value because most of the adsorbate is pseudomorphic. The thicker layers relax completely and they are likely to have a different stress release mechanism, which might be similar to what we discuss in Publication 4 and in the section 4.6.

Domain boundary networks have been observed with direct imaging methods in tensile Cu overlayers on Ru(0001) surfaces [72, 73, 74, 75]. The Ru substrate has hexagonal structure but the hcp(0001) surface has the same geometry as fcc(111) up to the second neighbor shell and consequently the two bimetallic systems are comparable. While on Ru(0001) the Cu adsorbate stays epitaxial beyond the coverage of one atomic layer, the appearance of the domain structure already in the submonolayer regime on Pd(111) is

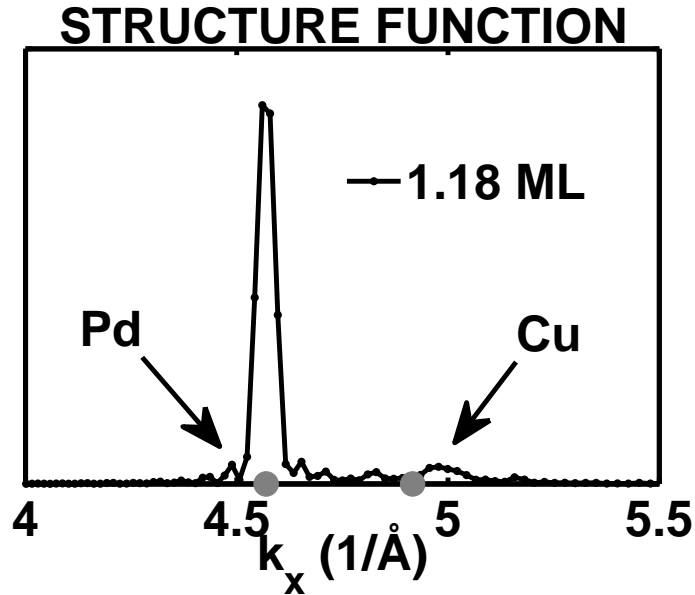


Figure 4.8: The structure function calculated for a single wetting film which has relaxed and formed stacking domains, as shown in Fig. 4.7. The gray dots show the positions of the peaks for ideal Pd and Cu lattices. The Cu peak is smeared and split into two because it comes from two kind of domain walls, as explained in section 4.2.

consistent with the 2% larger level of stress.

4.6 Relaxation of several overlayers

In Publication 4 we investigate fcc(111) overlayers with the simple modified Lennard-Jones potential by the activation-minimization procedure. Due to geometric restrictions, 2D systems have only a few kinds of defects. The 3D generalizations of the 2D defect motifs correspond to a stacking fault tetrahedron and to a set of complete close-packed rows forming a linear stacking fault with triangular cross-section. In Publication 4 we call these two dislocations as "localized" and "extended" defects.

The tetrahedron does not release much stress and according to our results, it is not among the most likely defects. The linear stacking fault on the other hand seems to release the stress almost completely. Because the simulation cell size we used was comparable to the defect size, we can only say that the extended defect seems to be the dominant stress release mechanism in the multilayer case. When we investigated the Cu/Pd(111) case with larger simulation cell sizes with EAM interactions, the large scale structure of the linear stacking faults resembled a triangular network.

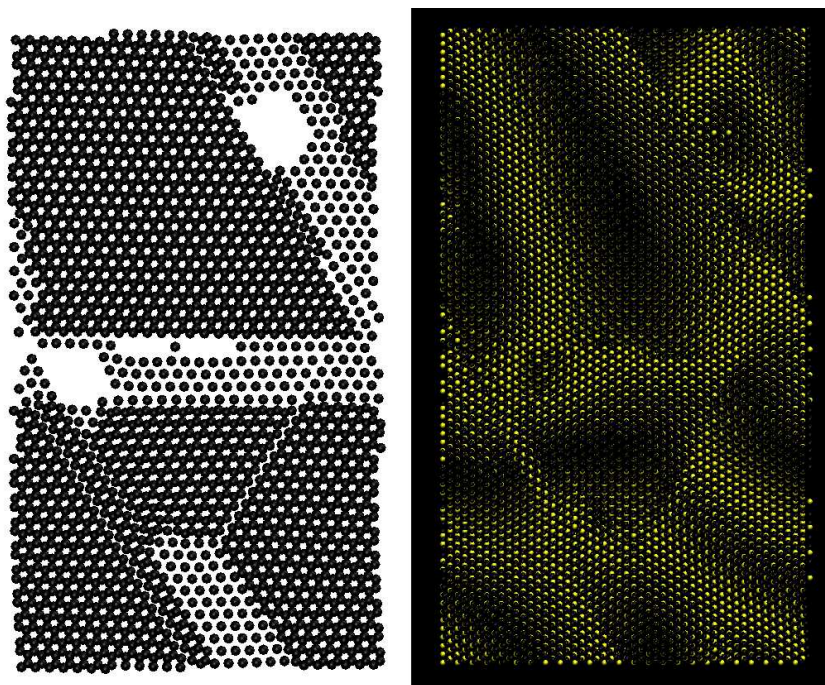


Figure 4.9: With a larger simulation cell size some rows from the top adsorbate layer sink to the layers below them, like the left panel which shows the two topmost adsorbate layers after RBP activation without tilting illustrates. This process corresponds to the appearance of an extended row dislocation network. In the right panel the background and the adsorbate are black while the substrate is plotted with a light color. Only in the hcp stacking the substrate is visible through the overlayer. This shows that the stacking domain structure may still be present in the multilayer case.

We also compared the energy barriers for different misfits and for different coverages with the same misfit. As expected, we find that the energy barrier decreases with the misfit if the defect nucleation takes place in the same fashion for all the misfits. For instance in the tensile case the largest barrier is typically in the beginning of the transition path and it corresponds to a local S-curve in a row on the topmost adsorbate layer. The same conclusion holds for the coverage dependence of the nucleation barrier.

When the nucleation started independently at several places, the final states are more disordered than with a single starting point. It should also be noted that at larger system sizes nucleation-induced local defects such as cracks become more abundant.

Chapter 5

Summary and outlook

In this thesis we have studied the atomic level processes of structural stress relaxation in heteroepitaxial overlayer systems at low coverages. Practically all bimetallic systems have a lattice mismatch but the unique property of heteroepitaxial overlayers is that the stress is strong enough to destabilize the film. Without the stress, the corresponding growth mode would be solely determined by the surface and interface energies.

In Publications 1 and 3 we use a modified Lennard-Jones model to look at the dependence of the growth modes and island shapes on the lattice mismatch and the surface and interface energies. Because most of the sophisticated many-body potentials are specifically fitted for their target materials, a simple Lennard-Jones model is particularly transparent and handy for this kind of qualitative study. With only two parameters it is easy to assign the cause of each effect to the corresponding physical process.

Publication 1 studies a model, where the misfit f is the only difference between the substrate and the adsorbate. The growth mode in this case would be the flat layer-by-layer mode if the stress did not destabilize the film. We relax all the convex 2D island shapes with neither overhangs nor keyholes and which are reflection symmetric about a line perpendicular to the substrate. By comparing the energies of the relaxed configurations we find that the most common shapes are truncated pyramids. In many cases there are short additional facets at the corners and in a few cases with high f there is a kink in the middle of the non-horizontal faces. We find that for small misfits the adsorbate prefers to be a flat epitaxial layer. After a certain fairly small coverage the adsorbate starts to adopt a several layers thick configuration with misfits above 4 %.

Because the stress in completely coherent islands increases with size, the structures have to nucleate dislocations at a certain critical size. In Publications 1 and 2 we create large pseudomorphic islands and look at the defect nucleation. As expected, defects are created at the bottom corners of the island and move along the adsorbate-substrate interface to the center of the bottom adsorbate layer. Publication 1 also studies the decay

of an unstable 11-atom island. The transition path has multiple sizable energy barriers and consequently such an island would probably stay in a kinetically trapped state for a relatively long time.

In Publication 1 we do not find the Stranski-Krastanov growth mode. This mode is interesting because it can accommodate the so called optimal island shapes and sizes, which ought to be coverage independent. In Publication 3 we vary the interface energy between the substrate and the adsorbate. As expected, stronger bonds between the materials increase the misfit requirements to get thicker adsorbate structures and vice versa. With submonolayer coverages we still see no indication of the Stranski-Krastanov growth mode. To study the higher coverage regime, we further restrict our island shapes to be truncated pyramids with short additional facets at the corners because according to our studies these are the most likely island shapes. We then fix the coverage to a few layers and map out the growth modes for misfits and interaction energies within a few percents from the values corresponding to equal adsorbate and substrate.

In Publications 3 and 4 we find that the Stranski-Krastanov growth mode exists between the Volmer-Weber and layer-by-layer modes when the interactions favor wetting. The result does not change when we repeat the same calculation for larger coverages. To get an answer to the optimal shape and size question in this model, we fix the misfit and the interface energy to values which correspond to the Stranski-Krastanov mode. With these parameters we vary the coverage and find that both the island width and the aspect ratio increase slowly with the coverage. Out of these, the island width seems to be the more inflexible geometrical factor.

To understand the energetics of the islands, we introduce an analytically calculable reference energy for the completely pseudomorphic configuration and compare the expression with the energies of numerically relaxed islands. It turns out that when the island width is varied while the height is kept constant, the relaxation becomes gradually localized near the non-horizontal faces while the bulk of the island stays pseudomorphic. In the large island width limit the difference between the reference energy and the numerically calculated energy tends asymptotically to a constant. For each height the width dependence is fitted to a hyperbola and the parameters of these fits are in the end fitted to the island heights. The resulting expression is capable of reproducing the numerically calculated growth modes and the island shape dependence on the coverage. The formula of Publications 3 and 4 shows that the energetics of coherent, supported 2D Lennard-Jones clusters can be understood in fairly simple terms.

Publication 4 discusses some similar Lennard-Jones studies on 3D overlayer systems. Previous overlayer studies on 2D systems had suggested that the most typical stress relaxation structure in that geometry is a triangular stacking faulted domain with one edge on the surface and the opposite corner at the substrate-adsorbate interface. By extension one could make the hypothesis that in 3D the typical structures would be tetrahedra or

ridges with a similar cross section. As expected, the energy barrier between the defect structures and the pseudomorphic state is found to decrease and eventually vanish with the misfit.

After the qualitative studies we focus on a particularly interesting catalytically active system Cu/Pd(111). Experimentally it is known that the copper overlayer does not alloy with the substrate below 450 K. The growth is estimated to be epitaxial below coverage of three atomic layers. After the limit coverage there is a transition to a complete relaxed state.

We abandon the Lennard-Jones interaction model in Publication 5. Instead, we use the Embedded Atom Method which has been shown to be able to give a realistic description for many properties of metals.

The results of Publication 5 reveal that the epitaxy of the adsorbate layer is lost already in the submonolayer coverage range. The structure of the overlayer is similar to the structure of Cu/Ru(0001) layers which have been studied in detail with direct imaging techniques. The Cu/Pd(111) system has not been analyzed in such a detail and we suggest a new interpretation for the existing experimental results. According to our calculations the adsorbate splits into fcc and hcp stacking domains in the submonolayer regime. Both domains have the lattice constant of the substrate. Stress relaxation takes place only near the domain boundaries and its contribution in the experimental data is very small in comparison to the bulk contribution. The qualitative results of Publication 4 and our other preliminary investigations suggest that when the coverage exceeds multiple complete atomic layers, the adsorbate density and the lattice constant can return to their equilibrium values. The extra material needed to accomplish this are taken from the uncomplete layers above through the adatom incorporation mechanism. In this light our results are not in contradiction with the experiments but rather encourage new experiments to examine the Cu/Pd(111) system with direct imaging techniques.

This series of studies is by no means complete. Many stress relaxation avenues such as alloying or nanowire formation were left largely unexplored. In this thesis we compare our 2D island results with 3D Lennard-Jones nanowires and find a surprisingly good match. Thus, we have a good reason to believe our approach can be generalized to 3D. However, in 3D islands the number of possible facets, defects, and shapes is much larger and there are many more effects which have to be taken into account. A natural but tedious extension of our Lennard-Jones results would be to repeat our activation-minimization treatment to a representative set of supported 3D clusters.

For specific systems the Embedded Atom Method is more reliable than our generic Lennard-Jones interaction model. The fcc(111) surfaces are generally expected to create highly regular stacking domain patterns. One direction for future work in this area could be to study these patterns for other bimetallic pairs which do not alloy. It has been speculated that such a regular domain pattern could serve as a template for further

self-assembling structures and in this kind of use knowledge on the properties of such structures might be useful.

We have compared the atomistic simulation results with the Phase Field Crystal model calculations both in the island and overlayer studies. The models seem to agree quite well. Because the latter model can escape atomistic time scale restrictions, it is a great tool for problems involving defects and elasticity. Recently, the Phase Field Crystal model has been shown to be applicable to 3D fcc and hcp crystals and in this light it would be an efficient and promising tool for finding plausible island and overlayer relaxation structures. Work in this direction is already in progress.

Appendix:

Chemical potential near a surface

Let the surface z_0 grow and become z_1 . We also assume for simplicity that both surfaces z_0 and z_1 have the same projection on (x, y) plane. In the same process the particle number of the cluster changes from N_0 to N_1 , the volume from V_0 to V_1 . We also assume that the crystal has the ideal lattice structure with constant number density $\rho = 1/v$.

In vacuum, where $p = 0$, the free energy changes by

$$(A.1) \quad F(z_1) - F(z_0) = \int_{N_0}^{N_1} \mu_0 dN + \int dxdy\phi \Big|_{z_1} - \int dxdy\phi \Big|_{z_0},$$

where ϕ is the surface free energy projected on (x, y) -plane. The first term can be written as

$$(A.2) \quad \int_{N_0}^{N_1} \mu_0 dN = \frac{\mu_0}{v} \int_{V_0}^{V_1} dV = \frac{\mu_0}{v} \int dxdy \int_{z_0}^{z_1} dz = \frac{\mu_0}{v} \int dxdy \int_0^1 ds \eta(x, y),$$

where $\eta(x, y) = z_1(x, y) - z_0(x, y)$. For this change of variables to be valid, we have to assume that the free energy difference does not depend on the growth path, or in other words that the process is reversible.

Along the growth path $z(x, y) = z_0(x, y) + s\eta(x, y)$ and integrands of the second and third terms of Eq. (A.1) can be written as

$$(A.3) \quad \begin{aligned} \int dxdy\phi \Big|_{z_1} - \int dxdy\phi \Big|_{z_0} &= \int dxdy \int_0^1 ds \frac{d}{ds} \phi(\partial_x(z_0 + s\eta), \partial_y(z_0 + s\eta)) \\ &= \int dxdy \int_0^1 ds \partial_x \eta \left(\frac{\partial \phi(\partial_x z, \partial_y z)}{\partial(\partial_x z)} \right) + \partial_y \eta \left(\frac{\partial \phi(\partial_x z, \partial_y z)}{\partial(\partial_y z)} \right) \\ &= \int dxdy \int_0^1 ds \nabla \cdot (\eta \nabla_{\nabla} \phi) - \int dxdy \int_0^1 ds \eta \nabla \cdot \nabla_{\nabla} \phi, \end{aligned}$$

where we have defined the symbol

$$(A.4) \quad \nabla_{\nabla} \equiv \left(\frac{\partial}{\partial(\partial_x z)}, \frac{\partial}{\partial(\partial_y z)} \right).$$

Because the integral over parameter s is independent of x - and y -coordinates, it can be interchanged with the area integral and the divergence term in Eq. (A.3) is

$$(A.5) \quad \begin{aligned} \int dxdy \int_0^1 ds \nabla \cdot (\eta \nabla_{\nabla} \phi) &= \int_0^1 ds \int dxdy \nabla \cdot (\eta \nabla_{\nabla} \phi) \\ &= \int_0^1 ds \oint_{z_1=z_0} \eta d\mathbf{l} \cdot \nabla_{\nabla} \phi = 0, \end{aligned}$$

where we have used the Stokes theorem and the assumption that z_0 and z_1 agree at the boundary of the projected surface area and therefore $\eta = 0$ along the whole integration curve.

When the terms are collected together, the free energy difference becomes

$$(A.6) \quad F(z_1) - F(z_0) = \int dxdy \int_0^1 ds \eta \left(\frac{\mu_0}{v} - \nabla \cdot \nabla_{\nabla} \phi \right) = \int_{N_0}^{N_1} dN (\mu_0 - v \nabla \cdot \nabla_{\nabla} \phi).$$

Because chemical potential

$$(A.7) \quad \mu = \frac{\delta F}{\delta N}$$

we see that the so called surface excess of the chemical potential is

$$(A.8) \quad \delta\mu = -v \nabla \cdot \nabla_{\nabla} \phi.$$

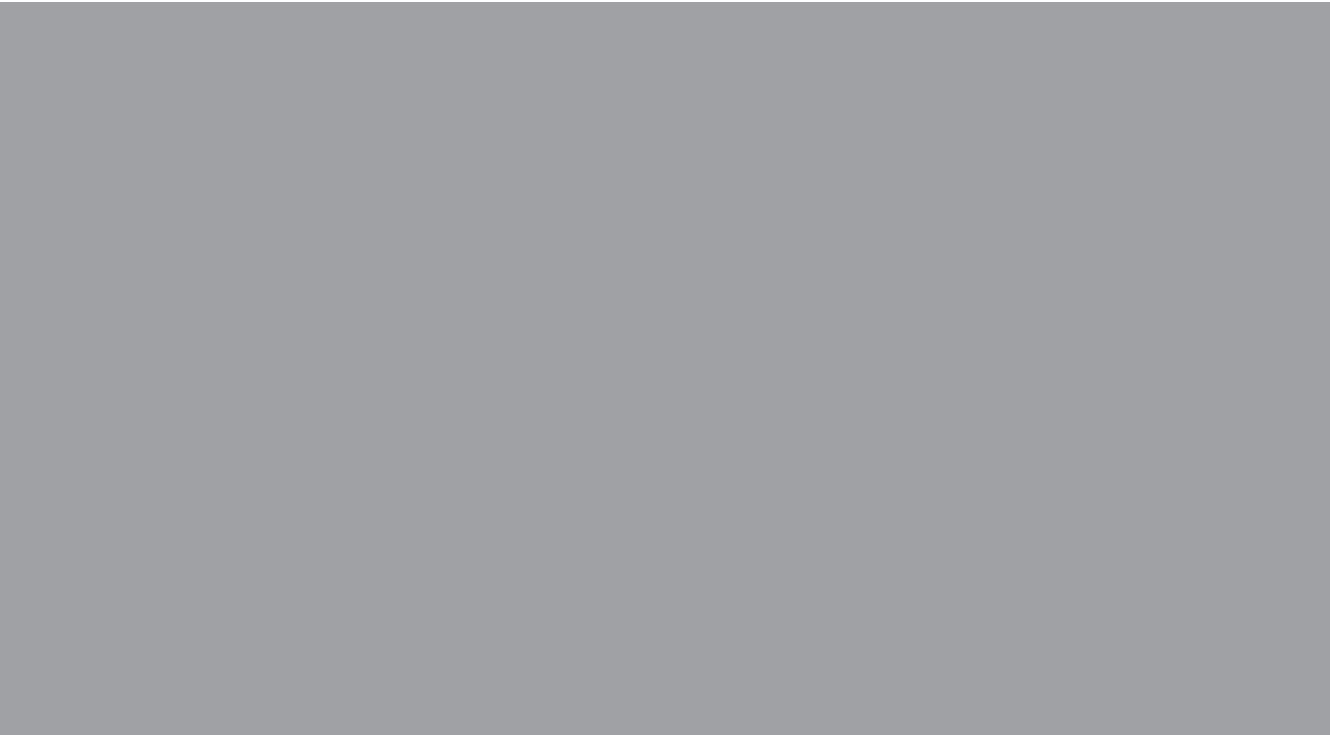
Bibliography

- [1] J. D. Aiken III, and R. G. Finke, *J. Mol. Catal. A: Chem.* **145**, 1 (1999).
- [2] M. Y. Lai, and Y. L. Wang, *Phys. Rev. B* **64**, 241404(R) (2001).
- [3] G. Rossi, A. Rapallo, C. Mottet, A. Fortunelli, F. Baletto, and R. Ferrando, *Phys. Rev. Lett.* **93**, 105503 (2004).
- [4] F. Baletto and R. Ferrando, *Rev. Mod. Phys.* **77**, 371 (2005).
- [5] E. Roduner, *Chem. Soc. Rev.* **35**, 583 (2006).
- [6] J. P. Wilcoxon and B. L. Abrams, *Chem. Soc. Rev.* **35**, 1162 (2006).
- [7] G. Rossi, and R. Ferrando, *Nanotechnology* **18**, 225706 (2007).
- [8] M. Kulmala, H. Vehkamäki, T. Petäjä, M. Dal Maso, A. Lauri, V.M. Kerminen, W. Birmili and P.H. McMurry, *J. Aerosol Sci.* **35**, 143 (2004).
- [9] T. Wang, X. Chen, G.Q. Lu, and G.Y. Lei, *J. Electron. Mater.* **36**, 1333 (2007).
- [10] P. O. Jubert, O. Fruchart and C. Meyer, *Phys. Rev. B* **64**, 115419 (2001).
- [11] O. Fruchart, P. O. Jubert, M. Eleoui, B. Borca, P. David, V. Santonacci, A. Liénard, M. Hasegawa and C. Meyer, *J. Phys.: Condens. Matter* **19**, 053001 (2007).
- [12] D. J. Eaglesham and M. Cerullo, *Phys. Rev. Lett.* **64**, 1943 (1990).
- [13] A. A. Golovin, M. S. Levine, T. V. Savina and S. H. Davis, *Phys. Rev. B* **70**, 235342 (2004).
- [14] I. Daruka and A.-L. Bara'bási, *Phys. Rev. Lett.* **79**, 3708 (1997).
- [15] N. Moll, M. Scheffler and E. Pehlke, *Phys. Rev. B*, **58**, 4566 (1998).
- [16] I. Daruka, J. Tersoff, and A.-L. Bara'bási, *Phys. Rev. Lett.* **82**, 2753 (1999).

- [17] K. Højrup Hansen, T. Worren, S. Stempel, E. Lægsgaard, M. Bäumer, H.-J. Freund, F. Besenbacher and I. Stensgaard, *Phys. Rev. Lett.* **83**, 4120 (1999).
- [18] N. Combe, P. Jensen and J.-L. Barrat, *Surf. Sci.* **490**, 351 (2001).
- [19] V. M. Kaganer and K. H. Ploog, *Phys. Rev. B* **64**, 205301 (2001).
- [20] C. H. Chiu, *Phys. Rev. B* **69**, 165413 (2004).
- [21] A. Pimpinelli, J. Villain, in *Physics of Crystal Growth*, (Cambridge University Press, Cambridge, 1998).
- [22] E. Hahn, E. Kampshoff, N. Wälchli, and K. Kern, *Phys. Rev. Lett.* **74**, 1803 (1995).
- [23] B. Oral and R.W. Vook, *J. Vac. Sci. Technol. A* **8**, 3048 (1990).
- [24] G. Liu, T. P. St. Clair and D. W. Goodman, *J. Phys. Chem. B* **103**, 8578 (1999).
- [25] A. de Siervo, R. Paniago, E.A. Soares, H.-D. Pfannes, R. Landers and G.G. Kleiman, *Surf. Sci.* **575**, 217 (2005).
- [26] H. C. Andersen, *J. Chem. Phys.* **72**, 2384 (1980).
- [27] H. J. C. Berendsen, J. P. M. Postma, W. F. van Gunsteren, A. DiNola, and J. R. Haak, *J. Chem. Phys.* **81**, 3684 (1984).
- [28] S. Zhen and G. J. Davies, *Phys. Stat. Sol. A* **78**, 595 (1983).
- [29] J. A. Rayne, *Phys. Rev.* **118**, 1545 (1960).
- [30] M. S. Daw and M. I. Baskes, *Phys. Rev. B* **29**, 6443 (1984).
- [31] S. M. Foiles, M. I. Baskes and M. S. Daw, *Phys. Rev. B* **33**, 7983 (1986).
- [32] M. Finnis and E. Sinclair, *Phil. Mag. A* **5**, 45 (1984).
- [33] Y. Lu, M. Przybylski, O. Trushin, W. H. Wang, J. Barthel, E. Granato, S. C. Ying and T. Ala-Nissila, *Phys. Rev. Lett.* **94**, 146105 (2005).
- [34] C. Mottet, G. Tréglia and B. Legrand, *Phys. Rev. B* **66**, 045413 (2002).
- [35] O. Trushin, E. Granato, S.-C. Ying, P. Salo and T. Ala-Nissila, *Phys. Stat. Sol. B*, **232**, 100 (2002).
- [36] O. Trushin, E. Granato, S.-C. Ying, P. Salo and T. Ala-Nissila, *Phys. Rev. B* **65**, 241408(R), (2002); *Phys. Rev. B* **68**, 155413 (2003).
- [37] O.S. Trushin, P. Salo, T. Ala-Nissila, and S.C. Ying, *Phys. Rev. B* **69**, 033405 (2004).

- [38] H. Jónsson, G. Mills and K. W. Jacobsen, in *Classical and Quantum Dynamics in Condensed Phase Simulations*, ed. by B. J. Berne *et al* (World Scientific, Singapore, 1998).
- [39] K. Elder and M. Grant, *Phys. Rev. E* **70**, 051605 (2004).
- [40] C. de Dominicis, *J. Math. Phys.* **3**, 983 (1962).
- [41] G. Ripka, *Phys. Rep.* **56**, 1 (1979).
- [42] K. R. Elder, N. Provatas, J. Berry, P. Stefanovic, and M. Grant, *Phys. Rev. B* **75**, 064107 (2007).
- [43] R. E. Miller and V. B. Shenoy, *Nanotechnology* **11**, 139 (2000).
- [44] E. Wong, P. E. Sheehan, and C. M. Lieber, *Science* **277**, 1971 (1997).
- [45] G. Parry, A. Cimetière, C. Coupeau, J. Colin, and J. Grilhé, *Phys. Rev. E* **74**, 066601 (2006).
- [46] P. Politi, G. Grenet, A. Marty, A. Ponchet, and J. Villain, *Phys. Reports* **324**, 271 (2000).
- [47] E. Pehlke, N. Moll, A. Kley and M. Scheffler, *Appl. Phys. A* **65**, 525 (1997).
- [48] C. D. Rudin and B. J. Spencer, *J. Appl. Phys.* **86**, 5530 (1999).
- [49] H.T. Johnson and L.B. Freund, *J. Appl. Phys.* **81**, 6081 (1997).
- [50] L.G. Wang, P. Kratzer, M. Scheffler and N. Moll, *Phys. Rev. Lett.* **82**, 4042 (1999).
- [51] L.G. Wang, P. Kratzer, N. Moll, and M. Scheffler, *Phys. Rev. B* **62**, 1897 (2000).
- [52] J. Goniakowski, A. Jelea, C. Mottet, G. Barcaro, A. Fortunelli, Z. Kuntová, F. Nita, A. C. Levi, G. Rossi, and R. Ferrando, *J. Chem. Phys.* **130**, 174703 (2009).
- [53] R. A. Budiman and H.E. Ruda, *J. Appl. Phys.* **88**, 4586 (2000).
- [54] C. Ratsch and A. Zangwill, *Surf. Sci.* **293**, 123 (1993).
- [55] V. A. Shchukin, A.I. Borovkov, N.N. Ledentsov and P.S. Kop'ev, *Phys. Rev. B* **51**, 17767 (1995).
- [56] V. I. Marchenko, *JETP Letters* **33**, 8, (1981).
- [57] B. J. Spencer, P. W. Voorhees, and J. Tersoff, *Phys. Rev. Lett.* **84**, 2449 (2000).
- [58] P. Thibault and L. J. Lewis, *Phys. Rev. B* **70**, 035415 (2004).

- [59] H. Uemura, M. Uwaha and Y. Saito, J. Phys. Soc. Japan **71**, 1296 (2002).
- [60] I. Daruka and J. Tersoff, Phys. Rev. B **66**, 132104 (2002).
- [61] B.J. Spencer and J. Tersoff, Phys. Rev. B **63**, 205424 (2001).
- [62] B.J. Spencer and J. Tersoff, Appl. Phys. Lett. **77**, 2533 (2000).
- [63] I. Daruka and A.-L. Barabási, Appl. Phys. Lett. **72**, 2102 (1998).
- [64] P. A. Huttunen, and A. Vehanen, Phys. Rev. B **42**, 11570 (1990).
- [65] T. K. Sham, J. Hrbek, and K.H. Tan, Surf. Sci. **236**, 259 (1990).
- [66] X. H. Feng, M. R. Yu, S. Yang, G. Meigs, and E. Garfunkel, J. Chem. Phys. **90**, 7516 (1989).
- [67] C. B. Carter and R. Q. Hwang, Phys. Rev. B **51**, 4730 (1995).
- [68] J. C. Hamilton and S. M. Foiles, Phys. Rev. Lett. **75**, 882 (1995).
- [69] P. Zeppenfeld, K. Kern, R. David and G. Comsa, Phys. Rev. B **38**, 3918 (1988).
- [70] O. Schaff, A. K. Schmid, N. C. Bartelt, J. de la Figuera and R. Q. Hwang, Mater. Sci. Eng., A **319**, 914 (2001)
- [71] R. Pushpa and S. Narasimhan, Phys. Rev. B **67**, 205418 (2003).
- [72] C. Günther, J. Vrijmoeth, R. Q. Hwang and R. J. Behm, Phys. Rev. Lett. **74**, 754 (1995).
- [73] R. Q. Hwang and M. C. Bartelt, Chem. Rev. **97**, 1063 (1997).
- [74] A. K. Schmid, N. C. Bartelt, J. C. Hamilton, C. B. Carter, and R. Q. Hwang, Phys. Rev. Lett. **78**, 3507 (1997).
- [75] J. de la Figuera, A. K. Schmid, N. C. Bartelt, K. Pohl and R. Q. Hwang, Phys. Rev. B **63**, 165431 (2001).
- [76] F. El Gabaly, W. L. W. Ling, K. F. McCarthy and J. de la Figuera, Science **27**, 1303 (2005).
- [77] G. Rossi and R. Ferrando, J. Phys.: Condens. Matter. **21**, 084208 (2009).
- [78] D. J. Wales, in *Energy Landscapes with Applications to Clusters, Biomolecules and Glasses*, (Cambridge University Press, Cambridge, 2003).
- [79] A. de Siervo, E. A. Soares, R. Landers and G. G. Kleiman, Phys. Rev. B **71**, 115417 (2005).



ISBN 978-952-60-3148-4
ISBN 978-952-60-3149-1 (PDF)
ISSN 1795-2239
ISSN 1795-4584 (PDF)